Epidermal maintenance of Langerhans cells relies on autophagy-regulated lipid metabolism

Florent Arbogast[1,2], Raquel Sal-Carro[1], Wacym Boufenghour[1], Quentin Frenger[2,9], Delphine Bouis[1], Louise Filippi De La Palavesa[1], Jean-Daniel Fauny[1], Olivier Griso[4], Hélène Puccio[4], Rebecca Fima[5], Thierry Huby[5], Emmanuel L. Gautier[5], Anne Molitor[3], Raphaël Carapito[3,6], Seiamak Bahram[3,6], Nikolaus Romani[7], Björn E. Clausen[8], Benjamin Voisin[1], Christopher G. Mueller[1], Frédéric Gros[1,2,9]*, Vincent Flacher[1]*

1 Laboratory CNRS I²CT/UPR3572 Immunology, Immunopathology and Therapeutic Chemistry, Strasbourg Drug Discovery and Development Institute (IMS), Institut de Biologie Moléculaire et Cellulaire, Strasbourg, France.

2 Université de Strasbourg, Strasbourg, France.

3 Laboratoire d'Immunorhumatologie Moléculaire, Plateforme GENOMAX, INSERM UMR_S 1109, Faculté de Médecine, Fédération Hospitalo-Universitaire OMICARE, ITI TRANSPLANTEX NG, Université de Strasbourg, 67085, Strasbourg, France. Strasbourg Federation of Translational Medicine (FMTS), Strasbourg University, Strasbourg, France.

4 INSERM U1258 / CNRS UMR7104, Institut de Génétique et de Biologie Moléculaire et Cellulaire, Illkirch, France.

5 Sorbonne Université, INSERM, UMR_S 1166 ICAN, Paris, France.

6 Service d'Immunologie Biologique, Plateau Technique de Biologie, Pôle de Biologie, Nouvel Hôpital Civil, Hôpitaux Universitaires de Strasbourg, Strasbourg, France.

7 Department of Dermatology, Venereology and Allergology, Medical University of Innsbruck, Innsbruck, Austria

8 Institute for Molecular Medicine and Paul Klein Center for Immunotherapy (PKZI), University Medical Center of the Johannes Gutenberg-University Mainz, Mainz, Germany.

9 Present address: INSERM UMR_S U1109 Immunorhumatologie Moléculaire, Fédération de Médecine Translationnelle de Strasbourg (FMTS) ITI Transplantex NG, Centre de Recherche en Biomédecine de Strasbourg (CRBS), Faculté des Sciences de la Vie, Université de Strasbourg, Strasbourg, France.

* Correspondance : f.gros@unistra.fr, v.flacher@ibmc-cnrs.unistra.fr

ABSTRACT (149 words)

Macroautophagy (often-named autophagy), a catabolic process involving autophagy-related (*Atg*) genes, prevents accumulation of harmful cytoplasmic components and mobilizes energy reserves in long-lived and self-renewing cells. Autophagy deficiency affects antigen presentation in conventional dendritic cells (DCs) without impacting their survival. However, previous studies did not address epidermal Langerhans cells (LCs), a proliferating skin DC subset with extended lifespan. Here, we demonstrate that deletion of either *Atg5* or *Atg7* in LCs leads to their gradual depletion. ATG5-deficient LCs showed metabolic dysregulation and accumulated neutral lipids. Despite increased mitochondrial respiratory capacity, they were unable to process lipids, eventually leading them to ferroptosis. Metabolically impaired LCs upregulated proinflammatory transcripts, in line with exacerbated inflammasome-dependent priming. Moreover, they decreased expression of neuronal interaction receptors, in line with a reduction of epidermal nerves upon LC depletion. Altogether, autophagy represents a critical regulator of lipid storage and metabolism in LCs, allowing their maintenance in the epidermis.

KEYWORDS

Autophagy, Langerhans cells, skin, homeostasis, lipid droplets, ferroptosis, metabolism

ABBREVIATIONS

2-NBDG: 2-(N-(7-Nitrobenz-2-oxa-1,3-diazol-4-yl) Amino)-2-Deoxyglucose

AMPK: AMP-activated protein kinase

APCs: Antigen-presenting cells

Atg: Autophagy-related genes

DCs: Dendritic cells

cDCs: Conventional dendritic cells

DETCs: Dendritic epidermal T cells

ER: Endoplasmic Reticulum

FCS: fetal calf serum

IRE1: Inositol-requiring enzyme 1

LCs: Langerhans cells

LN: Lymph nodes

MHC-II: Major histocompatibility complex

MT: Mitotracker

ROS: reactive oxygen species

UPR: Unfolded protein response

TGF-β1: Tumor growth factor β 1

Xbp1: X-box binding protein 1

Manuscript length: 38177 characters (without spaces, methods and references)

INTRODUCTION

Langerhans cells (LCs) are resident antigen-presenting cells (APCs) of the epidermis (Doebel et al., 2017; Kaplan, 2017). LCs arise from hematopoietic precursors that emerge from the yolk sac and the fetal liver to colonise the skin before birth (Hoeffel et al., 2012). There, they are maintained lifelong by local proliferation (Merad et al., 2002). LCs exhibit an exceptional longevity, with a half-life of several weeks, whereas other dendritic cells (DCs) are replenished from bone marrow precursors within days (Kamath et al., 2002). Possibly as a consequence of UV exposure, LCs are endowed with a potent DNA-repair capacity, allowing the survival of at least a pool of self-renewing cells upon gamma irradiation (Price et al., 2015). Despite free diffusion of glucose from the blood into the lowest layers of the epidermis, their position in the stratum granulosum implies a limited supply of nutrients, which must be metabolised in a very hypoxic environment (Bedogni et al., 2005). Similar to other cutaneous DC subsets, LCs migrate to lymph nodes (LNs) following microorganism recognition or irradiation. There, they contribute, as conventional dendritic cells (cDC), to antigen presentation and differentiation of $CD4^+$ and $CD8^+$ T cells, either driving immune activation or tolerance (Bedoui et al., 2009; Flacher et al., 2014; Igyarto et al., 2011). LCs are among the first APCs that sense skin infections (Kashem et al., 2015) and are involved in inflammatory disorders such as psoriasis (Singh et al., 2016). Therefore, a deeper understanding of their homeostasis appears critical.

Autophagy is a conserved mechanism of self-digestion, allowing the engulfment of cytoplasmic content into double-membrane vesicles, which fuse with lysosomes for degradation and recycling of the sequestered content (Arbogast et al., 2018; Clarke and Simon, 2018). The core autophagy proteins are encoded by autophagy-related (*Atg*) genes. Autophagy is promoted under energetic stress notably trough the inhibition of the PI3K/AKT/mTOR pathway (Galluzzi et al., 2014). Autophagy also contributes to metabolic equilibrium in homeostatic conditions as it is a key process to support energy provision. For cells relying on oxidative phosphorylation to generate ATP, autophagy contributes to maintain a functional mitochondrial pool through degradation of defective mitochondria and to mobilize fatty acids through degradation of lipid droplets in a process called lipophagy (Kim et al., 2014). To support homeostasis, autophagy also acts as a quality-control mechanism during the unfolded protein response (UPR), preventing the accumulation of misfolded protein aggregates and degrading excess or damaged endoplasmic reticulum (ER) (Anding and Baehrecke, 2017). These housekeeping forms of autophagy are

particularly important in long-lived and self-renewing cells. In the immune system, B-1 B cells, memory B and T cells as well as plasma cells rely on autophagy for their maintenance (Arbogast et al., 2018; Arnold et al., 2016; Clarke et al., 2018; Murera et al., 2018; Pengo et al., 2013; Xu et al., 2014). ATG proteins are also involved in several non-autophagic processes such as LC3-associated phagocytosis (LAP). LAP requires Rubicon (*Rubcn*) to form an initiation complex, and is involved in microorganism clearance, efferocytosis and antigen presentation, which are highly relevant for DCs (Heckmann and Green, 2019; Munz, 2015). Notably, autophagy impairment in DCs notably leads to defective $CD4^+$ and $CD8^+$ T cell responses (Alissafi et al., 2017; Lee et al., 2010; Mintern et al., 2015; Weindel et al., 2017).

Overall, selective deletion of *Atg* genes in macrophages and DCs has demonstrated that autophagy modulates pathogen resistance, antigen presentation, and proinflammatory signals, i.e. inflammasome activity (Bah and Vergne, 2017; Ghislat and Lawrence, 2018; Valecka et al., 2018; Takahama et al., 2018). Similarly, recent reports focused on LCs support a role of autophagy in the regulation of inflammatory responses (Müller et al., 2020; Said et al., 2014) and in the immune response against intracellular bacteria (Dang et al., 2019). Moreover, autophagy proteins participate in the intracellular routing of human immunodeficiency virus (HIV) particles towards degradative compartments in human LCs upon Langerin/CD207-mediated uptake (Ribeiro et al., 2016). Interestingly, enhancing autophagy by pharmacological agents limits HIV-1 mucosal infection and replication (Cloherty et al., 2021). Yet, non-autophagic roles of ATG proteins cannot be ruled out to explain these results.

Thus far, autophagy defects were only assessed in cDCs, in which antigen presentation, but not cell survival, was affected. (Lee et al., 2010; Mintern et al., 2015; Oh and Lee, 2019). No information is currently available on the consequences of constitutive autophagy impairment for LCs *in vivo*. Since LCs are self-renewing, long-lived APCs that are exposed to low availability of nutrients, UV irradiation or stress related to infection, we hypothesized that efficient autophagy might be a key element supporting their maintenance in the epidermis. To investigate this, we generated *Cd207*-specific deletion of *Atg5* in order to define primary roles of autophagy and related processes in LC biology.

RESULTS

ATG5 is necessary for Langerhans cell network maintenance.

Since evidence for autophagosomes in primary LCs has been so far limited (Ribeiro et al., 2016), we first verified whether LCs from digested murine epidermis comprise such compartments. Electron microscopy of LCs, including original images and reanalysis of previously published samples (Schuler and Steinman, 1985), allowed the identification of double-membrane compartments as well as crescent-shape structures reminiscent of incipient phagophores and isolation membranes. The diameter of the autophagosomes was between 400 and 600nm **(Figure S1)**. In line with this observation, LC3 staining by immunofluorescence revealed positive compartments within LCs **(Figure 1A, upper panels)**. When LCs were treated with hydroxychloroquine to block lysosomal degradation of autophagosomes, we observed an accumulation of membrane-associated LC3 by flow cytometry, thereby demonstrating autophagic flux **(Figure 1B, upper panel)**. Altogether, this showed constitutive autophagic activity in LCs of wild-type mice.

To determine the function of autophagy in LCs *in vivo* we generated *Cd207-cre x Atg5*$^{flox/-}$ (*Atg5*$^{\Delta Cd207}$) mice, in which the essential autophagy gene *Atg5* is deleted by CRE-mediated recombination in cells expressing CD207 **(Figure S2A)**. Efficiency of the deletion was verified by RT-qPCR of LCs sorted from the mouse epidermis **(Figure S2B)** and from skin-draining LNs of 4-week-old mice **(Figure S2C, D)**. This confirmed that the breeding strategy resulted in an optimal deletion efficiency, as *Atg5* mRNA was undetectable in LCs from *Atg5*$^{\Delta Cd207}$ mice, as compared with LCs from *Atg5*$^{flox/+}$ and *Cd207-cre x Atg5*$^{flox/+}$ control animals (respectively referred to as *Atg5*^{WT} and *Atg5*$^{WT/\Delta}$ below). With respect to migratory dermal DCs isolated from LNs of *Atg5*$^{\Delta Cd207}$ mice, *Atg5* mRNA was absent from CD103^{+} dermal cDC1, which also express CD207 (Henri et al., 2010), but, as expected, it was still present in CD207^{-} MHCII^{high} dermal DCs **(Figure S2D)**.

To address whether the deletion of *Atg5* leads to autophagy impairment in LCs, formation of autophagic compartments was assessed by LC3 immunostaining. LC3^{+} punctate staining in the cytoplasm of *Atg5*^{WT} LCs was clearly visible, whereas LC3 staining was diffuse in LCs from *Atg5*$^{\Delta Cd207}$ mice **(Figure 1A, lower panels, and Supplementary Videos SV1, SV2)**. This reflects the expected consequences of ATG5 deficiency, i.e. the absence of LC3 conjugation with phosphatidylethanolamine (LC3-II) and lack of integration into autophagic compartments. Since this accumulation of LC3^{+} vesicles may also reveal an impaired degradation of autophagosomes, the acidification and lysosomal load were quantified by

Lysosensor and Lysotracker probes, respectively. We could thus verify that it was unperturbed in the absence of ATG5 **(Figure S3)**. Finally, we observed that autophagic flux was abolished in LCs of *Atg5*$^{\Delta Cd207}$ mice **(Figure 1B, lower panel)**. This shows that ATG5 deletion leads to autophagy impairment in LCs.

To monitor the possible involvement of autophagy in the homeostatic maintenance of LCs under steady state conditions, we evaluated their epidermal network at different ages. Since CD207 expression in MHCII^{+} epidermal LC precursors is completed around 7-10 days after birth (Tripp et al., 2004), we assessed the proportion of MHCII^{+} TCRγδ^{-} CD207^{+} LCs among CD45^{+} epidermal cells by flow cytometry from 10 days until 9 months of age **(Figure 1C)**. The basal proportion of LCs at 10 days was comparable for mice of all genotypes, suggesting that no major defect occurs in the seeding of MHCII^{+} CD207^{-} embryonic LC precursors in the epidermis, which also corresponds to the expected kinetics of *Cd207* promoter activity and CRE expression (Tripp et al., 2004) **(Figure 1D)**. In *Atg5*^{WT} and *Atg5*$^{WT/\Delta}$ mice, we observed a moderate increase of LCs until 6-12 weeks, followed by a decrease in aging mice. Nevertheless, the proportion of LCs diminished sharply around 2-4 weeks of age in the epidermis of *Atg5*$^{\Delta Cd207}$, eventually stabilizing at around 5% of epidermal CD45^{+} leukocytes at 9 months.

To reinforce the conclusion that the loss of LCs is due to impaired autophagy and not other ATG5-related cellular homeostatic dysfunctions, we generated *Cd207-cre x Atg7*$^{flox/flox}$ (*Atg7*$^{\Delta Cd207}$) mice and compared their epidermal cell suspensions with that of *Atg7*$^{flox/flox}$ (*Atg7*^{WT}*)* mice. Similar to our findings with *Atg5*$^{\Delta Cd207}$ mice, ATG7 deficiency resulted in a significant depletion of LCs from the epidermis of mice older than 10 weeks **(Figure 1E)**. Thus, we can exclude effects only linked to ATG5, such as direct regulation of apoptosis independently of the autophagy machinery (Galluzzi et al., 2014). Additionally, we could exclude a role for LAP or other endocytic processes requiring ATG5, as the epidermal network of LCs appeared unaffected in Rubicon-deficient mice **(Figure S4).**

We then performed an immunofluorescent staining of the LC network in epidermal sheets prepared from ear skin of *Atg5*$^{\Delta Cd207}$ and control mice **(Figure 1F)**. We did not observe any obvious difference in the LC network in 3-week-old mice, regardless of their genotype. However, and in accordance with flow cytometry results, very few LCs were visible in 6-month-old *Atg5*$^{\Delta Cd207}$ mice. Interestingly, LCs remaining in older mice were often assembled in disseminated patches. This pattern is reminiscent of the network reconstitution that occurs through slow *in situ* LC proliferation following induced depletion in Langerin-DTR

mice (Bennett et al., 2005). Indeed, LCs ensure the integrity of their epidermal network by self-renewal (Chorro et al., 2009; Ghigo et al., 2013). Consequently, we assessed the proliferative capacity of ATG5-deficient LCs by 5-bromo-2'-deoxyuridine (BrdU) incorporation and Ki-67 staining by flow cytometry **(Figure 1G)**. We observed proliferation rates consistent with our previous observations in 4-week-old mice (Voisin et al., 2019), with comparable percentages of BrdU$^+$ and Ki-67$^+$ LCs in *Atg5*$^{\Delta Cd207}$ and control *Atg5*^{WT} mice, thereby concluding that autophagy deficiency does not prevent maintenance of the LC network by a major proliferative impairment. On the other hand, LCs of 6-month-old *Atg5*$^{\Delta Cd207}$ mice displayed higher proliferation rates, presumably because of homeostatic compensation for the depletion of their epidermal niche.

Finally, since dermal cDC1 also express CD207 and showed deletion of *Atg5* in *Atg5*$^{\Delta Cd207}$ mice **(Figure S2D)**, we quantified LC and cDC1 populations among total MHCII$^+$ CD11c$^+$ skin DCs. As expected, a decrease was evident for LCs present in whole skin suspensions, while the proportion of cDC1 among skin DCs was rather slightly increased **(Figure S5A,B)**. Thus, the core autophagic machinery is dispensable for the maintenance of dermal cDC1, yet appears essential to LCs.

ATG5-deficient Langerhans cells undergo apoptosis.

Since their self-renewal was not affected, the loss of ATG5-deficient LCs might be explained by an enhance emigration into lymph nodes or by increased cell death. LCs, as other DCs of peripheral tissues, undergo maturation and migrate to skin-draining LNs following inflammatory signals (Doebel et al., 2017; Kaplan, 2017). Alternatively, spontaneous maturation of LCs may result from disrupted TGF-β signalling, which, under physiological conditions, is required to maintain an immature state (Bobr et al., 2012; Kel et al., 2010). In both cases, an increased expression of maturation markers MHC-II and CD86 can be observed prior to the departure of LCs from the epidermis. We thus verified whether autophagy impairment might prompt spontaneous LC maturation. MHC-II and CD86 expression by LCs in the epidermis did not show any variation in *Atg5*$^{\Delta Cd207}$ compared to control mice **(Figure 2A, B)**. Moreover, because an overt LC emigration from the epidermis would lead to a noticeable accumulation in LNs, we determined LC numbers in inguinal and brachial LNs of 6-week-old mice. We observed instead a trend towards a decrease, only significant in percentage for LCs from *Atg5*$^{\Delta Cd207}$ mice **(Figure 2C, D)**. A similar pattern was observed for dermal cDC1 that also express CD207. As expected, no differences were detected for CD207$^-$ dermal DC subsets that lack ATG5 deletion. Taken together, these

results exclude that impaired autophagy leads to a massive spontaneous maturation and migration of LCs.

Finally, using flow cytometry, we addressed whether the absence of *Atg5* might lead to increased apoptosis by measuring the proportion of LCs with active caspase-3. Interestingly, this major effector of apoptosis was detected markedly induced in ATG5-deficient LCs, both in the epidermis and in LNs **(Figure 2E)**. Altogether, these results demonstrate that reduced cell division or increased maturation cannot account for LC network disintegration, whereas ATG5 appears crucial, even in the steady state, for LC survival.

ATG5-deficient Langerhans cells show limited endoplasmic reticulum stress.

Functional autophagy is required for the maintenance of the endoplasmic reticulum (ER). ER damage triggers the inositol-requiring enzyme 1 (IRE1)/X-box binding protein 1 (Xbp1) axis of the Unfolded Protein Response (UPR), which is a master regulator of DC survival and maturation (Cubillos-Ruiz et al., 2015; Grootjans et al., 2016; Tavernier et al., 2017). Autophagy regulates ER swelling, protein aggregation and thereby limits the extent of the UPR (Song et al., 2018). In line with this, exposure of wild-type LCs to the phosphatidylinositol-3-kinase inhibitor, wortmannin, which inhibits the initiation of the autophagosome formation, resulted in an increased labelling by ER-tracker **(Figure S6A)**. Therefore, we stained LCs from 3-week-old mice with ER-tracker, a fluorescent dye specific for ER membranes. Flow cytometry analysis showed a significantly increased ER-tracker staining in LCs of *Atg5*$^{\Delta Cd207}$ compared to wild-type mice **(Figure S6B)**. In line with this, confocal microscopy revealed an expanded ER compartment in these cells **(Figure S6C and Supplementary Videos SV3, SV4)**. These signs of ER expansion prompted us to study whether the expression of key intermediates of the UPR pathway might be elevated. Quantitative PCR was performed for *Ern1*, total *Xbp1*, spliced *Xbp1* and *Ddit3* mRNA. However, none of these genes showed increased expression, demonstrating that the UPR pathway was not constitutively engaged **(Figure S6D)**. Therefore, we conclude that ATG5-deficient LCs can cope with the observed ER swelling, which does not trigger a massive UPR that could lead to cell death.

Autophagy-deficient Langerhans cells accumulate intracellular lipid storage

To identify dysregulated gene expression patterns that could be linked with impaired autophagy, RNA sequencing was performed on epidermal LCs sorted from 3-week-old *Atg5*$^{\Delta Cd207}$ or *Atg5*^{WT} control mice. Analysis of *Atg5* mRNA sequencing reads confirmed the deletion of exon 3 in LCs upon CRE-mediated recombination **(Figure S7A)**. Principal

component analysis revealed clear differences in transcriptomic profiles between *Atg5*$^{\Delta Cd207}$ and *Atg5*^{WT} mice **(Figure S7B)**. Differentially expressed genes in *Atg5*$^{\Delta Cd207}$ LCs included 673 upregulated and 629 downregulated genes **(Table 2, Figure S7C, D)**. Gene ontology pathway enrichment analysis suggested in particular a dysregulation of cellular metabolism (GO:0046942, GO:0043269, GO:0044272, GO:0051186, GO:0046085, GO:1901615, GO:0015711, GO:0009166, GO:0007584; **Figure S7E)**.

Autophagy regulates cellular lipid metabolism by lipophagy, which has a crucial role in balancing energy supply in both steady state and under metabolic stress. Lipophagy mediates lysosomal degradation of proteins that coat cytoplasmic lipid droplets, and lipolysis of triglycerides, thus liberating free fatty acids to be consumed by beta-oxidation in mitochondria (Kounakis et al., 2019). Accordingly, LCs of *Atg5*$^{\Delta Cd207}$ mice modulated the expression of several genes encoding actors of lipidic metabolism pathways **(Figure 3A)**. We noticed upregulation of mRNA of the solute carrier (SLC) family transporters MCT-4/SLC16A3 (lactate), SLC7A11 (cystein, glutamate) and SLC7A2 (lysine, arginine), which import molecules that directly or indirectly provide substrates to the tricarboxylic acid cycle. Upregulated expression of *Acss1* and *Acss2* (Acyl-CoA Synthetase Short Chain Family Member 1 and 2) is expected to favour synthesis of Acetyl-CoA, which can either be converted into lipids or fuel mitochondrial beta-oxidation. Fatty acid synthesis and energy storage in the form of lipid droplets appears to be favoured in ATG5-deficient LCs, as hinted by the upregulation of *Gyk*, encoding the Glycerol kinase which catalyses triglyceride synthesis, and *Acsl3,* encoding the Acyl-CoA Synthetase Long Chain Family Member 3, a key enzyme for neutral lipid generation (Gao et al., 2019).

To determine whether lipid storage was deregulated in autophagy-deficient LCs, epidermal cell suspensions were exposed to Bodipy, a lipid staining dye that targets neutral lipid-rich vesicles, which then can be quantified by flow cytometry. We first validated this experimental approach by treating wild-type LCs with etomoxir, a carnitine palmitoyltransferase I inhibitor that blocks the import of activated free fatty acids (acyl-CoA) by mitochondria. As expected, etomoxir treatment resulted in a stronger intensity of Bodipy staining, reflecting higher neutral lipid storage **(Figure 3B)**. Interestingly, treating LCs with the autophagy inhibitor wortmannin also resulted in an increased Bodipy staining suggesting constitutive lipophagy in LCs **(Figure 3C)**. We then found that *Atg5*$^{\Delta Cd207}$ LCs retained more Bodipy as compared with LCs of control mice **(Figure 3D)**. We consistently observed by confocal microscopy that LCs of *Atg5*$^{\Delta Cd207}$ contained more Bodipy-positive

vesicular structures that could correspond to lipid droplets **(Figure 3E and Supplementary Videos SV5, SV6)**. Perilipin-1 staining in LCs allowed to unequivocally identify lipid droplets, confirming that autophagy deficiency resulted in an abnormal increase in neutral lipid storage **(Figure 3F)**. Thus, enlargement of the ER may be a direct consequence of lipid droplets budding from this compartment.

Disrupted lipid metabolism in autophagy-deficient Langerhans cells

ATG5 deficiency might lead to an accumulation of intracellular lipids if energy production in LCs strongly relies on lipophagy to mobilize these storage units and produce energy by the beta-oxidation pathway (Kounakis et al., 2019). To assess the energy production in LCs, we focused on AMP-activated protein kinase (AMPK), a master regulator of energetic metabolism, which is phosphorylated on residues T183/T172 when ATP/AMP ratios decline (Herzig and Shaw, 2018). As measured by flow cytometry, AMPK phosphorylation was indeed increased in LCs from *Atg5*$^{\Delta Cd207}$ mice **(Figure 4A)**. Downstream of AMPK phosphorylation, import of glucose to support glycolysis, or fatty acid uptake and synthesis can be induced to help restore optimal ATP production. To quantify the glucose uptake intensity, we first monitored the expression of the glucose transporter GLUT-1 by LCs. However, no difference could be observed between LCs of *Atg5*$^{\Delta Cd207}$ mice and control mice **(Figure 4B)**. Next, we quantified the glucose uptake of these cells using 2-(N-(7-Nitrobenz-2-oxa-1,3-diazol-4-yl) Amino)-2-Deoxyglucose (2-NBDG), a fluorescent glucose analogue which can be tracked by flow cytometry. In line with the unmodified GLUT-1 expression, autophagy-deficient LCs were not more efficient at capturing glucose than LCs of wild-type mice **(Figure 4C)**. On the other hand, LCs from *Atg5*$^{\Delta Cd207}$ mice exhibited a stronger expression of CD36 **(Figure 4D)**. This scavenger receptor has a key role in the capture of free fatty acids and lipids, which was indeed increased when LCs incubated with Bodipy-labelled C16 fatty acid **(Figure 4E)**. Altogether, these assays demonstrate that autophagy-deficient LCs show a deficit in energy production, despite an increased ability to capture and store lipids.

To evaluate whether a lack of autophagy affects oxidative phosphorylation in LCs, we quantified metabolic flux of LCs exposed to a series of inhibitors of mitochondrial respiratory complexes **(Figure 4F).** The decrease of oxygen consumption rates for wild-type and ATG5-deficient LCs upon oligomycin treatment was similar to that of bone marrow-derived DCs (BMDCs), indicating a similar basal production of ATP at steady state **(Figure 4G: ATP)**. Wild-type LCs and BMDCs also displayed a comparable profile after exposure to

FCCP, which unleashes the maximal respiratory capacity of a cell. On the other hand, LCs of *Atg5*$^{\Delta Cd207}$ mice reacted to FCCP by a strikingly prominent peak of their oxygen consumption **(Figure 4G: Max)**. This implies that, in the absence of autophagy, the potential of LCs to mobilize oxidative phosphorylation, also called spare respiratory capacity, had massively increased **(Figure 4G: SRC)**. Despite this, ATG5-deficient LCs appeared unable to use this capacity to promote ATP production **(Figure 4G: ATP)**. The respiratory capacity of a cell relies on mitochondria, and transcriptome analysis demonstrated that mitochondria-related genes were differentially regulated upon loss of autophagy **(Figure 4H)**. Thus, we performed a double staining with mitotracker (MT) Green and Deep Red on LCs extracted from 3-week-old mice. While MT Deep Red is sensitive to mitochondrial membrane potential, MT Green stains mitochondrial membranes independently of the membrane potential, thus allowing normalization of the membrane potential to the mitochondrial load. An increased mitochondrial mass was detected **(Figure 4I)**, in line with the increased capacity of energy production that we measured by the mitochondrial stress assay. ATG5-deficient LCs did not display decreased membrane potential **(Figure S8A),** suggesting that mitochondrial function was preserved. Mitophagy is a key process to eliminate defective mitochondria, in particular when they produce reactive oxygen species (ROS). We used Mitosox staining to quantify ROS produced under altered mitochondria function, but this assay did not reveal any difference between *Atg5*$^{\Delta Cd207}$ and *Atg5*^{WT} mice **(Figure S8B)**. All things considered, since mitochondria and lysosomes of autophagy-deficient LCs remained functional, we conclude that shortage in the lipophagy-dependent fatty acid supply could not be compensated by increased mitochondrial mass.

Ferroptosis results from lipid oxidation in ATG5-deficient Langerhans cells

Mitosox detects superoxide O2·-, yet other ROS may cause cellular damage and death, i.e. H_2O_2 and HO·. Interestingly, ATG5-deficient LCs showed upregulated transcription of *Gss* (Glutathione-S Synthetase), *Slc7a11* (Cysteine/glutamate antiporter xCT), *Esd* (S-formylglutathione hydrolase) and *Gclm* (Glutamate-Cysteine Ligase Modifier Subunit), which are key elements in the glutathione-dependent response to ROS **(Figure 4J)**. The glutathione pathway is notably involved in preventing ferroptosis, in which cell death occurs as a consequence of iron-dependent lipid peroxidation (Stockwell, 2022). In favour of this hypothesis, we noticed several genes that showed significant moderate or high (more than two-fold) upregulation in ATG5-deficient LCs. These genes included ferroptosis-related genes such as *Hfe* (Homeostatic iron regulator), *Tfrc* (Transferrin receptor protein 1), *Ftl1*

(Ferritin Light Chain), *Slc7a1* (Solute Carrier Family 7 Member 1), *Sat1* (Spermidine/Spermine N1-Acetyltransferase 1), *Lpcat3* (Lysophosphatidylcholine Acyltransferase 3). Finally, elevated expression of *Ptgs2* (Prostaglandin-Endoperoxide Synthase 2/Cyclooxygenase 2), and *Acsl4* (acyl-CoA synthetase long-chain family member 4) is considered as a strong indication of ongoing ferroptosis.

To confirm that lipid peroxidation occurs in the absence of functional autophagy, LCs were exposed to Bodipy-C11, a derivative of undecanoic acid that emits fluorescence upon oxidation. As expected, upon treatment with this compound, LCs harvested from *Atg5*$^{\Delta Cd207}$ mice displayed significantly higher fluorescence intensity than LCs of *Atg5*^{WT} mice **(Figure 4K)**. Thus, our results indicate that oxidation of the lipids accumulated in ATG5-deficient LCs leads them to ferroptosis, thereby contributing to their progressive depletion from the epidermis.

Langerhans cells under metabolic stress alter cutaneous homeostasis

Besides metabolic imbalance, RNA sequencing revealed dysregulation of inflammation-related genes **(Figures S6E and 5A)**. In particular, autophagy-deficient LCs increased their expression of mRNA encoding IL-1α and chemokines CXCL1, CXCL2 and CXCL3, known to attract neutrophils through CXCR2. Despite this observation, no obvious signs of inflammation were observed on the skin of *Atg5*$^{\Delta Cd207}$ mice: when analysing ear skin of 3-week-old mice for myeloid infiltrates **(Figure 5B)**, the proportions of Gr1^{+} Ly6G^{+} neutrophils or Gr1^{low} Ly6G^{-} monocytes did not differ between *Atg5*^{WT} and *Atg5*$^{\Delta Cd207}$ mice **(Figure 5C)**. Since NRLP3, a key inflammasome component, was markedly upregulated in LCs of *Atg5*$^{\Delta Cd207}$ mice, we challenged this pathway by injecting intradermally a small dose of alum hydroxide into the ears of 3-week-old mice. In *Atg5*^{WT} mice, this resulted in only a modest increase of neutrophils **(Figure 5C)**, whereas monocytes were not significantly attracted **(Figure 5D)**. In contrast, alum hydroxide injection was able to drive monocyte infiltration into the ears of *Atg5*$^{\Delta Cd207}$ mice **(Figure 5D;** fold increases: x2.95 for *Atg5*^{WT} and x8.86 for *Atg5*$^{\Delta Cd207}$). This outcome suggests that the presence of autophagy-deficient LCs increases sensitivity to proinflammatory challenge.

Several reports showed that a long-term absence of LCs leads to a decrease of intraepidermal nerve endings, although the pathways governing this remains unidentified (Zhang et al., 2021; Doss and Smith, 2014). Interestingly, autophagy-deficient LCs downregulated a set of genes involved in neuronal interactions and axonal guidance (GO:0045664, GO:0050808, GO:0071526, GO:0030031; **Figures S6E and 5E)**. Thus, we

sought to investigate the epidermal neuronal network of mice aged 6 months and older. Since neuronal development is particularly sensitive to autophagy impairment (Hara et al., 2006), we chose to compare the density of LCs and epidermal sensory neurons of *Atg5*^{WT} and *Atg5*$^{\Delta Cd207}$ mice with that of heterozygous *Atg5*$^{WT/-}$ mice **(Figure 5F)**. As expected for mice of this age, we observed a decrease in LC density in *Atg5*$^{\Delta Cd207}$ epidermis, but not in control mice **(Figure 5G)**. In parallel, quantification of β3-tubulin staining demonstrated that only *Atg5*$^{\Delta Cd207}$ mice presented significantly less epidermal nerve endings as compared to *Atg5*^{WT} mice, although a slight reduction was observed in *Atg5*$^{WT/-}$ mice **(Figure 5H)**. Intriguingly, there was a stronger correlation of LC numbers with the density of epidermal nerve endings in *Atg5*$^{WT/-}$ and *Atg5*^{WT} mice than in *Atg5*$^{\Delta Cd207}$ mice with complete deletion of *Atg5* in LCs **(Figure S9).** This may imply that the remaining autophagy-deficient LCs were unable to support neuronal epidermal growth, in line with their decreased neuron-related transcripts. Altogether, in accordance with previous findings, LCs appear to play a crucial role in the extension of sensory neurons into the epidermis. Furthermore, the metabolic stress resulting from reduced autophagy may have an impact on the epidermal neuronal network.

DISCUSSION

In contrast to other types of DCs, epidermal LCs self-renew to maintain their population and they are exposed in the steady state to environmental conditions (hypoxia, irradiation) that may favour autophagy. We report here a major role for autophagy in LC homeostasis. When deprived of the key autophagy mediator ATG5, LCs displayed clear signs of lipid-related metabolic stress and underwent progressive depletion from the epidermis. They enhanced cutaneous immune infiltration upon inflammasome priming, and showed decreased transcription of innervation regulators, which is in accordance with a decreased network of epidermal nerves when these mice were aging.

The depletion of LCs was not due to their emigration or decreased proliferation, suggesting cell death as the most likely explanation. Our analyses excluded a significant contribution of the ER stress response and major mitochondrial damages. In the absence of autophagy, ferroptosis, implied from the upregulation of relevant detoxification pathways, was a consequence of uncontrolled supply of lipids and their peroxidation by ROS. Apoptosis may also occur in a relatively low proportion of ATG5-deficient LCs, as a result of the critically low ATP:AMP ratio (Liang et al., 2007) revealed by increased phosphorylation of AMPK.

The similar depletion of LCs observed using *Cd207*-specific *Atg7* deletion supports the idea

that ATG5-dependent, non-autophagic functions, are not directly involved in the maintenance of LCs. We could also rule out lysosomal alterations or the impairment for endocytic mechanisms such as LAP, since the LC network appeared unperturbed in *Rubcn*$^{-/-}$ mice. The importance of autophagy for other skin DC subsets *in vivo* has been investigated previously. An earlier report did not find any consequence on the maintenance for CD207^{+} cDC1, in line with our findings (Lee et al., 2010), although the absence of Vps34, which plays a role in autophagy and other biological pathways, resulted in the depletion of splenic cDC1 (Parekh et al., 2017). Recently, LAP in dermal cDC2 was found to be required to limit inflammation after UV exposure, without reported consequences on their homeostasis (Sil et al., 2020). Nevertheless, the ontogeny and features of LCs differ strikingly from those of other DC subsets (Doebel et al., 2017). Surprisingly, LCs had a continuous presence in skin-draining LNs, despite their depletion from the epidermis. This could be due to LCs remaining proliferative in older mice , which allowed the steady-state flux of LCs towards LNs to be kept constant. Emigration to LNs also entails a major environmental change as compared to the epidermis, and this may be beneficial to extended survival of LCs.

The metabolic requirements of LCs have never been studied and can only be extrapolated from those of keratinocytes nearby. In the epidermal layer where they reside, LCs are distant from dermal blood capillaries and have limited access to glucose and oxygen. Interestingly, epidermal hypoxia appears to regulate the functional properties of human LCs (Pierobon et al., 2016). Hypoxic tissues exhibit low levels of phosphorylated Akt (Bedogni et al., 2005), which is expected to promote autophagy. LCs attempted to compensate autophagy impairment by inhibiting the PI3K/Akt pathway: they decreased expression of Inositol-3-phosphate synthase 1 (*Isyna1*) and of TNF-α-induced protein 8-like protein 3 (*Tnfaip8l3*), which shuttles PIP2 and PIP3 across the plasma membrane (Fayngerts et al., 2014), whereas Protein Kinase C beta (*Prkcb*) was upregulated.

Although historically autophagy has been shown to be regulated through mTOR complex (in particular under energetic stress), it is now clear that several induction pathways coexist with constitutive activity, especially in immune cells. Intriguingly, progressive disappearance of epidermal LCs at a young age has been reported in mice with selective disruption of critical intermediates of the mTOR pathway (Kellersch and Brocker, 2013; Sparber et al., 2015, 2014). Therefore, since mTOR is recognized as a negative regulator of autophagy, it could be interpreted that excessive autophagy is detrimental to LCs. However, autophagy

has not been investigated in these mouse models. In addition, mTOR regulates many other cellular processes and, beyond autophagy, is critical to survival, lysosomal trafficking or cytokine signalling pathways. By impairing the recycling of receptors through lysosomes, LAMTOR2 deletion leads to a defect in TGF-β signalling, which is essential for the differentiation of LCs (Kaplan et al., 2007). Moreover, LCs deficient in Raptor, an adaptor of the mTOR complex 1, leave the epidermis, which may also result from an impaired TGF-β signalling that normally maintains the epidermal LC network by restricting their spontaneous migration to skin-draining LNs (Kel et al., 2010; Bobr et al., 2012). Altogether, there is no direct evidence to date that the deleterious impact of genetic ablations affecting the mTOR pathway in LCs may depend solely on altered autophagy.

ATG5-deficient LCs displayed an accumulation of lipid droplets that likely resulted from impaired lipophagy. Of note, a similar phenotype was recently reported for LCs of psoriatic lesions in both patients and mouse models (Zhang et al., 2022). In the absence of autophagy, LCs did not promote glycolysis and were unable to take advantage of their increased respiratory capacity linked to higher mitochondrial mass, highlighting the critical importance of lipophagy for their energy production. The limited ER swelling observed in our model, which was not sufficient to trigger the UPR pathway in LCs, may be related to defective energy mobilisation from lipid storage (Cubillos-Ruiz et al., 2015; Velázquez et al., 2016), multiple budding of lipid droplets (Gao et al., 2019) or modification of ER membrane dynamics following lipid peroxidation (Agmon et al., 2018). Accumulation of lipid droplets as a result of an impaired autophagy machinery has been observed in other cell types that rely on lipophagy. This catabolic process is key in the development of neutrophils (Riffelmacher et al., 2017). Of note, DCs derived from *Atg5*$^{-/-}$ bone marrow display elevated CD36 expression and lipid droplets, although no cell death was reported during the time frame of this *in vitro* experiment (Oh and Lee, 2019). Yet, the lifespan of bone marrow-derived or conventional DCs is not comparable to that of LCs, for alterations in lipid metabolism may have deleterious consequences when they accumulate in the long term. Considering that CD207 is expressed in LCs about 10 days after birth (Tripp et al., 2004), the time period at which LC depletion becomes visible (around 20 days of age) suggests that they cannot survive more than 2 weeks to autophagy deficiency in the steady state. This represents a relatively short delay as compared to other, unrelated cell types previously found to rely on autophagy, i.e. B-1 B cells that survive 6 weeks after deletion of *Atg5* (Clarke et al., 2018).

Some features of LCs are reminiscent of tissue-resident macrophages (Doebel et al., 2017).

Although autophagy regulates many functions of macrophages, it was not considered to play a prominent role in their homeostatic maintenance (Wu and Lu, 2019). It was only recently reported that a lack of autophagy affects the survival of a subset of peritoneal macrophages (Xia et al., 2020). Interestingly, similar to steady-state LCs, this subset is of embryonic rather than monocytic origin. It remains to be demonstrated whether the dependence on autophagy can be associated with the origin and/or long-term residency for macrophages within other organs.

The consequences for the epidermis of a long-term absence of LCs have been investigated through constitutive diphtheria toxin-mediated depletion in the huLangerin-DTA mouse strain (Su et al., 2020; Zhang et al., 2021). However, since LCs are absent from birth, it is difficult to identify which of the genes that they normally express may affect epidermal homeostasis. Here, we were able to document transcriptome alterations of ATG5-deficient LCs that are still present in young mice, albeit in a metabolically stressed state. First and foremost, our data suggested a potential for supporting inflammation. Immune infiltration did not occur spontaneously, which could be explained by the fact that autophagy-deficient LCs progressively disappear, limiting their capacity to induce inflammation. Nevertheless, a challenge by inflammasome agonist alum hydroxide resulted in a larger immune infiltration, especially involving monocytes, in mice where LCs were impaired for autophagy. Secondly, several genes involved in neuronal interactions were downregulated by ATG5-deficient LCs, including EPH receptor A1, Semaphorin 4A, Neuropilin-1 and Neuregulin-1. The long-term absence of LCs in our model led to a decrease of epidermal nerve endings. These findings thus represent a milestone for future investigations on neuroimmune interactions, considering the putative role of LCs and dermal macrophages (Kolter et al., 2019) in regulating sensory neuron growth and repair in the skin.

Altogether, we shed light on the metabolic adaptations of LCs that ensure their long-lasting tissue residency. It will be of great interest to translate these findings in the context of human skin diseases, considering that lipid supply and autophagy capacity of LCs may perturb their homeostasis and favour inflammation.

MATERIAL AND METHODS

Mice

Mice were bred and maintained on a C57BL/6J background at the animal facility of the Institut de Biologie Moléculaire et Cellulaire (IBMC). *Atg5*$^{flox/flox}$ and *Cd207-cre* mice were gifted by N. Mizushima and B.E. Clausen, respectively (Hara et al., 2006; Zahner et al., 2011). *Atg5*$^{+/-}$ mice were generated at the IBMC (Arnold et al., 2016). [*Atg5*$^{+/-}$; *Cd207-cre*] were obtained from a first cross between *Cd207-cre* and *Atg5*$^{+/-}$, then bred to *Atg5*$^{flox/flox}$ to obtain [*Atg5*$^{flox/-}$; *Cd207-cre*] (*Atg5*$^{\Delta Cd207}$) and littermates [*Atg5*$^{flox/+}$; *Cd207-cre*] (*Atg5*$^{WT/\Delta}$) and [*Atg5*$^{flox/+}$] (*Atg5*^{WT}). Mice were genotyped for their *Atg5* allele and the *Cd207-cre* transgene as previously described (Arnold et al., 2016; Zahner et al., 2011). All mice were bred and maintained in accordance with guidelines of the local institutional Animal Care and Use Committee (CREMEAS).

Antibodies and reagents for flow cytometry and immunofluorescence microscopy

Antibody stainings for flow cytometry or immunofluorescent microscopy were performed in SE buffer (Fetal Calf Serum 2%, EDTA 2.5mM). All reagents and antibodies are listed in **Table 1.**

Cell preparation and culture

Lymph nodes: Brachial and inguinal lymph nodes were digested for 1h at 37°C under shaking in R2 buffer (RPMI-1640 medium containing L-glutamine (Lonza) plus 2% fetal calf serum (Dutscher)) supplemented with 50µg/mL DNAse and 10µg/mL collagenase D (Roche).

Digestion of back skin epidermis (electron microscopy, LC proportions, caspase-3 activation, proliferation assays): Back skin was incubated with 0.5% Trypsin (VWR) for 45min at 37°C. After removal of the dermis, the epidermis was teased apart with forceps, followed by 15min of gentle shaking on a rotating wheel. Where indicated, CD11b^{+} LCs were enriched by magnetic bead separation (Miltenyi-Biotec).

Ear skin digestion (skin DC subsets, quantification of immune infiltrates): Ear skin were cut into small pieces, digested in R2 buffer containing 0.15mg/ml LiberaseTM and 0.12mg/ml DNAse (Roche) for 45min at 37°C and filtered through 100µm cell strainers.

Epidermal crawl-out assay (Bodipy C16 and glucose uptake, in vitro treatment with inhibitors, Seahorse assay): Back skin was incubated overnight at 4°C in R2 buffer, containing 1mg/mL dispase II (Roche). The separated epidermis was then laid upon cell

culture medium (RPMI medium supplemented with 10% fetal calf serum, 50mM β-Mercaptoethanol, (Gibco), 1% Gentamicin (Gibco), and 10mM HEPES (Lonza)) in a Petri dish for 24h at 37°C, allowing emigration of LCs.

Bone marrow-derived DCs: Femurs and tibias were collected from C57BL/6 mice. Bone marrow was flushed out, red blood cells lysed, filtered and cultured for 7 days in complete RPMI medium (RPMI-1640 medium containing L-glutamine plus 10% fetal calf serum) containing 20ng/mL recombinant GM-CSF (Peprotech).

Induction of cutaneous inflammation

For each mouse, one ear was injected intradermally with 25µL of 100µg/mL alum hydroxide (Roche), and the contralateral ear was left untreated. 4h later, whole skin was digested and cell suspensions were monitored by flow cytometry for $CD45^+$ $CD3^-$ $CD11b^+$ $Gr1^+$ $Ly6G^+$ neutrophils and $CD45^+$ $CD3^-$ $CD11b^+$ $Gr1^+$ $Ly6G^-$ monocytes.

Electron microscopy

Epidermal cell suspensions (freshly isolated or cultured for 3 days) were processed for electron microscopy essentially as described (Cavinato et al., 2017). Briefly, after pre-enrichment on bovine serum albumin density gradient, cells were washed and fixed using Karnovsky's formaldehyde-glutaraldehyde fixative for 1h at room temperature. Specimens were post-fixed in aqueous 3% osmium tetroxide and contrasted with 0.5% veronal-buffered uranyl acetate. Dehydration of samples was done in graded series of ethanol concentrations, followed by embedding in Epon 812 resin. Ultrathin sections were mounted on nickel grids, contrasted with lead citrate and examined by transmission electron microscopy (Phillips EM 400; Fei Company Electron Optics, Eindhoven, The Netherlands) at an operating voltage of 80kV. LCs were identified within epidermal cell suspensions by their electron-lucent cytoplasm, the absence of keratin tonofilament bundles, the presence of cytoplasmic processes (dendrites) and their ultrastructural hallmarks, the Birbeck granules.

Autophagy flux assessment by flow cytometry.

Measurements of autophagy fluxes were carried out using the Guava Autophagy LC3 Antibody-based Detection Kit (Luminex). LCs isolated through epidermal crawl-outs were cultured 18h at 37°C with or without the lysosome inhibitor provided with the kit (60 µM hydroxychloroquine). After labelling by FVD450, cells were stained for CD45, I-A/I-E, and TCRγ/δ. Cells were permeabilized with 0.05% saponin (Merck Millipore) to wash out the cytosolic LC3-I, then membrane-associated LC3 (LC3-II) was preferentially stained with

anti-LC3 FITC (clone 4E12). Flow cytometry analysis allowed to calculate autophagy fluxes, dividing the LC3-FITC mean fluorescence intensities of treated cells by that of untreated cells.

Glucose uptake

Cells obtained by crawl-out were glucose-starved for 24h in PBS (Lonza) supplemented with 0.5% fetal calf serum for 8 hours. Cells were then incubated for 30min at 37°C with 150µM of 2-[N-(7-nitrobenz-2-oxa-1,3-diazol-4-yl) amino]-2-deoxy-D-glucose (ThermoFisher).

Pharmacological inhibitions

Cells obtained by crawl-out were incubated for 24h at 37°C with the phosphatidylinositol-3-kinase inhibitor wortmannin or the carnitine palmitoyltransferase-1 inhibitor etomoxir (both from Sigma-Aldrich)**,** at 10 and 200µM respectively.

5-bromo-2'-deoxyuridine incorporation

1mg of 5-bromo-2'-deoxyuridine (BrdU; Sigma) was administered by intraperitoneal injection 72 hours prior to analysis. Drinking water also contained 0.8mg/mL BrdU. Following staining of surface markers CD45, I-A/I-E and TCRγδ, epidermal single-cell suspensions were fixed with Cytofix/Cytoperm buffer (BD Biosciences) and permeabilized with permeabilization buffer (BD Biosciences). DNA was then denatured with a DNAse solution (100µg/mL, BD Biosciences) to improve the accessibility of the incorporated BrdU to the detection antibody.

Quantitative real-time RT-PCR analysis

RNA was extracted from cells sorted from lymph nodes on a FACS Aria cell sorter (BD Biosciences) with RNeasy microKit (Qiagen). cDNA was obtained with Maxima Reverse Transcriptase Kit (ThermoFisher) using a T100 Thermal cycler (Biorad). Quantitative real-time PCR was performed on cDNA using Taqman preAmp MasterMix and Taqman Universal Mastermix (ThermoFisher) and Assays-on-Demand probes (*Gapdh*: Mm03302249_g1; *Atg5: Mm00504340_m1*). Each sample was amplified in triplicate in a StepOnePlus real-time PCR system (Applied Biosystems). mRNA levels were calculated with the StepOne v2.1 software (Applied Biosystems), using the comparative cycle threshold method, and normalized to the mean expression of *Gapdh* housekeeping gene.

Immunofluorescence microscopy of epidermal sheets

Ear epidermis was separated from the dermis by ammonium thiocyanate digestion (0.15M) for 20min at 37°C. Alternatively, for optimal preservation of neuronal networks, epidermal sheets were separated after 10mM EDTA diluted in PBS for 1h. Epidermis was then fixed by incubation in PBS 4% PFA or in glacial acetone for 15min at 4°C followed by incubation with PBS 5% BSA 0.1% Triton. Primary antibodies were incubated overnight at 4°C. After fixation, epidermal sheets were washed four times in blocking buffer consisting in 5% BSA in PBS for 15 minutes each time at room temperature. Sheets were then incubated overnight at 4°C with the primary antibodies: anti-β3-tubulin and AF647 anti-CD207 diluted in blocking buffer. After washing the sheets as described above, they were incubated with a solution of goat anti-mouse AF594, and 4',6-diamidino-2-phenylindole (DAPI) in blocking buffer for 1h at room temperature. After additional washings, epidermal sheets were mounted in Fluoromount-G mounting medium (ThermoFisher) and observed under a confocal microscope (Yokogawa Spinning Disk, Zeiss). Whole-mount epidermal images were processed using the open-source software FIJI to measure the total analysed area for each sample and to quantify the mean fluorescence intensity.

Immunofluorescence microscopy of epidermal cell suspensions

Cell suspensions were deposited on Lab-Tek chamber slides (Thermo Scientific Nunc) previously coated with a poly-L-Lysine solution (Sigma-Aldrich) diluted in ultra-pure water at 0.02% (v/v) to enhance cellular adhesion. Epidermal cells were then incubated with Mitotracker, Mitosox, ER-tracker, Bodipy or Bodipy-C16 according to the manufacturer's instructions (Invitrogen), before fixation using 2% PFA in PBS for 15min at RT. DAPI was incubated 15min at RT. Tissues were mounted and observed under a confocal microscope (Yokogawa Spinning Disk, Zeiss).

RNA sequencing

Total RNA was isolated from 10^5 sorted LCs with the RNeasy Mini Kit (Qiagen). RNA integrity was evaluated on an Agilent Bioanalyzer 2100 (Agilent Technologies). Total RNA Sequencing libraries were prepared with SMARTer® Stranded Total RNA-Seq Kit v2 - Pico Input Mammalian (TaKaRa) according to the manufacturer's protocol. Briefly, random priming was used for first strand synthesis and ribosomal cDNA has been cleaved by ZapR v2 in the presence of mammalian R-probes V2. Libraries were pooled and sequenced (paired-end 2*75bp) on a NextSeq500 using the NextSeq 500/550 High Output Kit v2 according to the manufacturer's instructions (Illumina). For analysis, quality control of each sample was carried out and assessed with the NGS Core Tools FastQC

(http://www.bioinformatics.babraham.ac.uk/projects/fastqc/). Sequence reads were mapped on the GRCm38 reference genome using STAR (Dobin et al., 2013) and unmapped reads were remapped with Bowtie2 (Langmead and Salzberg, 2012) using a very sensitive local option to optimize the alignment. The total mapped reads were finally available in BAM (Binary Alignment Map) format for raw read counts extraction. Read counts were found by the HTseq-count tool of the Python package HTSeq (Anders et al., 2015) with default parameters to generate an abundance matrix. At last, differential analyses were performed using the DEseq2 (Love et al., 2014) package of the Bioconductor framework. Differentially expressed genes between *Atg5*$^{\Delta Cd207}$ and *Atg5*^{WT} were selected based on the combination of adjusted p-value < 0.05 and FDR < 0.1. Pathway enrichment analysis was performed using Metascape (https://metascape.org) (Zhou et al., 2019).

Metabolic parameter quantitation by extracellular flux assay

CD45^{+} MHCII^{+} CD207^{+} CD103^{-} TCR□□$^{-}$ LCs were sorted from epidermal crawl-out suspensions on a FACSFusion cell sorter (Becton-Dickinson). Purified LCs or BMDCs (2.10^{5} cells/well) were seeded in Seahorse XF96 culture plate coated with poly-lysine (Sigma). After overnight culture, a Mitochondrial Stress Test was performed. In this assay, culture wells are injected sequentially with different inhibitors of the mitochondrial respiration. Energy production resulting from mitochondrial respiration was determined after each injection by measuring oxygen consumption rates (OCR, pmoles/min) on a Seahorse XF96 according to the manufacturer's instructions (Agilent). Oligomycin (OM) injection allowed calculating the oxygen consumption used for mitochondrial ATP synthesis. Carbonyl cyanide 4-(trifluoromethoxy)phenylhydrazone (FCCP) uncoupled mitochondrial respiration, allowing to calculate maximal respiration and spare respiratory capacity. Finally, rotenone (ROT) and antimycin A (AA) blocked mitochondrial complex I and III to determine the non-mitochondrial oxygen consumption. The following metabolic parameters were calculated:

ATP production = $OCR_{baseline} – OCR_{OM}$

Maximum respiration = $OCR_{FCCP} – OCR_{AA+ROT}$

Spare respiratory capacity (SRC) = $OCR_{FCCP} – OCR_{baseline}$

Lipid peroxidation assay

Upon enrichment in CD11b^{+} epidermal cells using magnetic bead separation (Miltenyi-Biotec), at least 50 000 cells were seeded and incubated for 10min at 37ºC with 2mM Bodipy-C11 (581/591) (4,4-difluoro-5,7-dimethyl-4-bora-3a,4a-diaza-s-indacene-3-

undecanoic acid; Invitrogen) in PBS. Cells were then resuspended in SE buffer and incubated with the following antibodies: CD3e-PerCP-Cy5.5, MHC-II-AF700 and CD45-APC-Cy7. Upon gating on $CD45^+$ CD3- $MHCII^+$ cells, the fluorescence of Bodipy-C11 was collected from the FITC channel on a Gallios cytometer (Beckman-Coulter).

Quantification of the density of epidermal nerve endings

The open-source software iLastik was used to segmentate images of whole-mount epidermal sheets stained for β3-tubulin and CD207, using machine learning to differentiate background from b3-tubulin signal. Images were then processed using the open-source software FIJI to measure the total area of each scan, as well as the area that was determined positive for b3-tubulin.

Statistical analyses

Statistical significance was calculated with the indicated tests using Prism software (GraphPad, versions 6-9). All data were presented as mean ± standard error of the mean (SEM). P-values < 0.05 were considered statistically significant (*, p<0.05, **, p<0.01, ***, p<0.001, ****,p<0.0001).

FUNDING

This work was funded by the French Centre National de la Recherche Scientifique, the Laboratory of Excellence Medalis (ANR-10-LABX-0034), EquipEx program I2MC (ANR-11-EQPX-022), Strasbourg University, Fondation Arthritis Courtin, ANR ERAPerMed BATMAN (ANR-18-PERM-0001), ANR AUTOMATE (ANR-20-CE15-0018-01) and Strasbourg's Interdisciplinary Thematic Institute (ITI) for Precision Medicine, TRANSPLANTEX NG, as part of the ITI 2021-2028 program of the University of Strasbourg, CNRS and INSERM, funded by IdEx Unistra (ANR-10-IDEX-0002) and SFRI-STRAT'US (ANR-20-SFRI-0012). Florent Arbogast and Delphine Bouis were recipients of pre-doctoral fellowships from the Ministère de la Recherche et de l'Enseignement Supérieur. Benjamin Voisin was supported by Marie Slodowska-Curie Individual Fellowship (H2020-MSCA-IF-2019 896095 VirIVITES).

AKNOWLEDGEMENTS

We thank Pr. Noboru Mizushima for his gift of *Atg5*$^{flox/flox}$ mice, Delphine Lamon and Fabien Lhericel for mouse breeding at the IBMC animal facility, and Claudine Ebel and Muriel Philipps at the cell sorting facility of the IGBMC.

AUTHOR CONTRIBUTIONS

F.A, F.G. and V.F. designed the research.

N.R. contributed electron microscopy images.

B.E.C. , E.L.G. and T.H. contributed essential reagents and critically reviewed the paper

F.A, D.B., W.B., R.S.-C., Q.F., L.F., R.F., F.G. and V.F. performed the experiments.

O.G. and H.P. helped design and analyze the metabolic measurement assays

R.C., A.M., S.B. and B.V. designed and analyzed the RNA sequencing assay

F.A, W.B., R.S.-C, J.-D.F., F.G. and V.F. analyzed the data.

F.A, C.G.M., F.G. and V.F. wrote the paper.

Figure legends

Figure 1: ATG5 deficiency in Langerhans cells disrupts autophagosomes and depletes their epidermal network. (A) Representative immunofluorescent stainings of MAP1LC3B (LC3) on LCs obtained by *in vitro* emigration from epidermal sheets of *Atg5*^{WT} **(Supplementary Video SV1)** and *Atg5*$^{\Delta Cd207}$ **(Supplementary Video SV2)** mice. Scale bars: 10µm. **(B)** Representative histogram plot of LC3β staining and quantification of mean fluorescence intensity for LCs of 3-week-old *Atg5*^{WT} and *Atg5*$^{\Delta Cd207}$ mice, treated or not with the lysosomal acidification inhibitor chloroquine. Autophagy flux was calculated as a ratio between mean fluorescence intensity for LC3β in treated and untreated cells. Data are presented as mean ±SEM, with each point corresponding to one individual mouse. Statistical analysis was performed using Mann-Whitney U test (***, $p<0.001$). **(C)** Representative dot plots (pre-gated on live CD45$^+$ cells) for the identification of MHCII$^+$ TCRγδ$^-$ Langerhans cells (LCs; all CD207$^+$) and MHCII$^-$ TCRγδ$^+$ dendritic epidermal T Cells (DETCs) in freshly digested back skin epidermal suspension of 6-month-old *Atg5*^{WT} and *Atg5*$^{\Delta Cd207}$ mice. **(D)** Comparison over time of the percentage of LCs among live CD45$^+$ epidermal cells for control (*Atg5*^{WT} and *Atg5*$^{WT/\Delta}$) and *Atg5*$^{\Delta Cd207}$ mice. Data are presented as mean ±SEM, with each point corresponding to n≥4 mice per time-point. Statistical analysis was performed using two-way ANOVA followed by Tukey's multiple comparison test. Only significant differences between *Atg5*^{WT} and *Atg5*$^{\Delta Cd207}$ mice are shown (****, $p<0.0001$). **(E)** Percentage of LCs among live CD45$^+$ cells in freshly digested back skin epidermis of 10-20 week-old *Atg7*^{WT} and *Atg7*$^{\Delta Cd207}$ mice. Data are presented as mean ±SEM, with each point corresponding to one individual mouse. Statistical analysis was performed using Mann-Whitney U test (***, $p<0.001$). **(F)** Representative immunofluorescent staining of CD207 on epidermal sheets of ear skin from 3-week (upper panels) and 6-month-old (lower panels) *Atg5*^{WT} and *Atg5*$^{\Delta Cd207}$ mice. Scale bars: 100µm. **(G)** Percentages of epidermal LCs expressing the proliferation markers 5-bromo-2'-deoxyuridine (BrdU) and Ki-67 for 4-week (upper panels) and 6-month-old (lower panels) *Atg5*^{WT} and *Atg5*$^{\Delta Cd207}$ mice. Data are presented as mean ±SEM, with each point corresponding to one individual mouse. Statistical analysis was performed using Mann-Whitney U test (**, $p<0.01$; ns, $p>0.05$).

Figure 2: ATG5-deficient LCs undergo apoptosis. (A) CD86 and **(B)** MHC-II mean fluorescence intensity for epidermal LCs of control (*Atg5*^{WT} and *Atg5*$^{WT/\Delta}$) and *Atg5*$^{\Delta Cd207}$ mice. Data are presented as mean ±SEM, with each point corresponding to one individual

mouse. Statistical analysis was performed using Kruskal-Wallis one-way ANOVA followed by Dunn's multiple comparison test (ns, p>0.05). **(C)** Percentages and **(D)** absolute numbers of LCs, cDC1 and CD207$^-$ DCs in freshly digested skin draining lymph nodes of control (*Atg5*^{WT} and *Atg5*$^{WT/\Delta}$) and *Atg5*$^{\Delta Cd207}$ mice. Data are presented as mean ±SEM, with each point corresponding to one individual mouse. Statistical analysis was performed using Mann-Whitney U test (*, p<0.05; ns, p>0.05). **(E)** Percentage of cells with activated caspase-3 in LCs of freshly digested back skin epidermis (left panel) and LCs, cDC1 and CD207- dermal DCs of skin-draining lymph nodes (right panel) for control (*Atg5*^{WT} and *Atg5*$^{WT/\Delta}$) and *Atg5*$^{\Delta Cd207}$ mice. Data are presented as mean ±SEM, with each point corresponding to one individual mouse. Statistical analysis was performed using Kruskal-Wallis one-way ANOVA followed by Dunn's multiple comparison test (*, p<0.05; **, p<0.01; ns, p>0.05).

Figure 3: Impaired autophagy increases the lipid storage compartments of Langerhans cells. (A) Differentially expressed transcripts related to lipid metabolism in *Atg5*^{WT} vs. *Atg5*$^{\Delta Cd207}$ LCs. **(B-D)** Flow cytometry quantification of the Bodipy mean fluorescence intensity in epidermal LCs obtained from C57BL/6 mice then treated with **(B)** etomoxir or **(C)** wortmannin, or **(D)** from control (*Atg5*^{WT} and *Atg5*$^{WT/\Delta}$) and *Atg5*$^{\Delta Cd207}$ mice. Data are presented as mean ±SEM, with each point corresponding to one individual mouse. Statistical analysis was performed using Kruskal-Wallis one-way ANOVA followed by Dunn's multiple comparison test (*, p<0.05; **, p<0.01; ns, p>0.05). **(E-F)** Representative immunofluorescent stainings of CD207$^+$ epidermal LCs obtained from *Atg5*^{WT} (upper panels) and *Atg5*$^{\Delta Cd207}$ (lower panels) mice and stained with Bodipy **(E and Supplementary Videos SV5 and SV6)** or anti-Perilipin-1 antibody **(F)**. Scale bars: 10µm.

Figure 4: Impaired lipid metabolism leads ATG5-deficient LCs to ferroptosis (A-E) Flow cytometry quantification of mean intensity of fluorescence for **(A)** Phosphorylated AMPK, **(B)** GLUT1, **(C)** 2-NDBG uptake, **(D)** CD36 and **(E)** Bodipy C16 uptake in epidermal LCs obtained from control (*Atg5*^{WT} and *Atg5*$^{WT/\Delta}$) and *Atg5*$^{\Delta Cd207}$ mice. Data are presented as mean ±SEM, with each point corresponding to one individual mouse. Statistical analysis was performed using Kruskal-Wallis one-way ANOVA followed by Dunn's multiple comparison test (*, p<0.05; **, p<0.01; ns, p>0.05). **(F)** Epidermal LCs sorted from *Atg5*^{WT} or *Atg5*$^{\Delta Cd207}$ mice and BMDCs from C57BL/6 mice were sequentially exposed to Oligomycin (OM), Carbonyl cyanide 4-(trifluoromethoxy)phenylhydrazone (FCCP), rotenone (ROT) and antimycin A (AA), and oxygen consumption rates (OCR) were measured by a

Seahorse XF96 analyzer throughout the experiment. Data are from one representative experiment out of three. **(G)** ATP production ($OCR_{baseline}$ – OCR_{OM}), maximum respiration (Max; OCR_{FCCP} – OCR_{AA+ROT}) and spare respiratory capacity (SRC; OCR_{FCCP} – $OCR_{baseline}$) were calculated from the OCR curves Data are presented as mean ±SEM, with each point corresponding to a pool of individual mice. Statistical analysis was performed using two-way ANOVA followed by Šídák's multiple comparisons test (*, p<0.05; ***, p<0.001; ns, p>0.05). **(H)** Differentially expressed transcripts related to mitochondrial function in $Atg5^{WT}$ vs. $Atg5^{\Delta Cd207}$ LCs. **(I)** Mitochondrial load for epidermal LCs of *$Atg5^{WT}$*, *$Atg5^{WT/\Delta}$* and *$Atg5^{\Delta Cd207}$* mice, as measured by mean fluorescence intensity of Mitotracker Green staining. Data are presented as mean ±SEM, with each point corresponding to one individual mouse. Statistical analysis was performed using Kruskal-Wallis one-way ANOVA followed by Dunn's multiple comparison test (*, p<0.05; **, p<0.01; ns, p>0.05). **(J)** Differentially expressed transcripts related to ferroptosis in $Atg5^{WT}$ vs. $Atg5^{\Delta Cd207}$ LCs. **(K)** Quantification of lipid peroxidation for epidermal LCs of control (*$Atg5^{WT}$* and *$Atg5^{WT/\Delta}$*) and *$Atg5^{\Delta Cd207}$* mice, as measured by mean fluorescence intensity of Bodipy-C11. Data are presented as mean ±SEM, with each point corresponding to one individual mouse. Statistical analysis was performed using Kruskal-Wallis one-way ANOVA followed by Dunn's multiple comparison test (*, p<0.05; ns, p>0.05).

Figure 5: Langerhans cells under metabolic stress have impaired tissue homeostasis function.

(A) Differentially expressed genes in *$Atg5^{WT}$* vs. *$Atg5^{\Delta Cd207}$* LCs: transcripts related to immune function. **(B)** One ear of *$Atg5^{WT}$ or $Atg5^{\Delta Cd207}$* mice was injected intradermally with 2.5µg alum hydroxide and the contralateral ear was left untreated. 4h later, whole skin was digested and cell suspensions were monitored by flow cytometry for $CD45^+$ $CD3^-$ $CD11b^+$ $Gr1^+$ $Ly6G^+$ neutrophils and $CD45^+$ $CD3^-$ $CD11b^+$ $Gr1^{low}$ $Ly6G^-$ monocytes. **(C,D)** Percentage of neutrophils **(C)** and monocytes **(D)** among live $CD45^+$ cells. Data are presented as mean ±SEM, with each point corresponding to one individual mouse. Statistical analysis was performed using Mann-Whitney U tests for unpaired comparison between mice, and Wilcoxon tests for paired comparison of alum-treated vs. untreated ears (*, p<0.05; **, p<0.01; ***, p<0.001; ns, p>0.05). **(E)** Differentially expressed genes in *$Atg5^{WT}$* vs. *$Atg5^{\Delta Cd207}$* LCs: transcripts related to neuronal interactions. **(F)** Representative immunofluorescence microscopy image of epidermal sheets obtained from ears of *$Atg5^{WT}$* and *$Atg5^{\Delta Cd207}$* mice and stained with antibodies against β3-tubulin (neurons) and CD207

(LCs). Scale bar: 50µm. Quantification in *Atg5*^{WT}, *Atg5*$^{WT/-}$ and *Atg5*$^{\Delta Cd207}$ mice: **(G)** Number of CD207^{+} LCs per mm². **(H)** Relative area of β3-tubulin staining. Data are presented as mean ±SEM, with each point corresponding to one field of view (n=3 mice per condition). Statistical analysis was performed using Kruskal-Wallis one-way ANOVA followed by Dunn's multiple comparison test (**, $p<0.01$; ****, $p<0.0001$; ns, $p>0.05$).

Supplementary figures

Figure S1: Autophagosomes are detectable in murine Langerhans cells. (A) Transmission electron microscopy of LCs in a bulk epidermal cell suspension freshly isolated from C57BL/6 mice (far right panel) or cultured for 3 days. The inset image highlights a Birbeck granule (arrow). **(B)** Close-up micrographs of autophagic structures corresponding to the boxes in the low power overview micrographs. 1 and 3 appear to be limiting membranes of incipient autophagy; 2 and 4 show double membrane-limited autophagosomes. Scale bars: 1µm (A); 500nm (B).

Figure S2: *Atg5* is efficiently deleted in Langerhans cells and dermal cDC1 of *Atg5*$^{\Delta Cd207}$ mice. (A) Representative electrophoresis of genotyping PCR. Left panel: floxed, wild-type (WT) and exon 3-deleted (KO) alleles of *Atg5*. Right panel: wild-type and *Cre* knock-in alleles of *Cd207*. **(B)** *Atg5* mRNA expression in sorted epidermal CD45+ MHCII+ TCRγδ^{-} LCs from control (*Atg5*^{WT} and *Atg5*$^{WT/\Delta}$) and *Atg5*$^{\Delta Cd207}$ mice. Fold changes were calculated relative to mRNA expression in LCs of *Atg5*^{WT} control mice. Data are presented as mean ±SEM, with each point corresponding to one individual mouse. Statistical analysis was performed using Kruskal-Wallis one-way ANOVA followed by Dunn's multiple comparison test (*, $p<0.05$; ns, $p>0.05$). **(C)** Gating strategy used to sort lymph nodes MHC-II^{+} CD207- FSA high dermal DCs (dDCs), MHC-II^{+} CD207^{+} CD103^{-} LCs (LCs) and MHC-II^{+} CD207^{+} CD103^{+} cDC1 (CD103^{+}). Red dots in the top panel depict backgating of CD207^{+} LCs/cDC1. **(D)** *Atg5* mRNA expression in LCs, cDC1 and CD207- dDCs sorted from pooled lymph node cell suspensions of at least 3 control (*Atg5*^{WT} and *Atg5*$^{WT/\Delta}$) or *Atg5*$^{\Delta Cd207}$ mice. Fold changes were calculated relative to mRNA expression in cells of *Atg5*^{WT} control mice. ND, not detectable.

Figure S3: ATG5-deficient LCs have functional lysosomes. Representative half-set overlay of LysoTracker-Red (left panel) and LysoSensor (right panel) stainings and comparison of the ratio of mean fluorescence intensities of each marker for epidermal LCs of control (*Atg5*^{WT} and *Atg5*$^{WT/\Delta}$) and *Atg5*$^{\Delta Cd207}$ mice. Data are presented as mean ±SEM, with each point corresponding to one individual mouse. Statistical analysis was performed using Kruskal-Wallis one-way ANOVA followed by Dunn's multiple comparison test (ns, $p>0.05$).

Figure S4: Rubicon deficiency does not alter the Langerhans cell network. (A) Percentage of CD45^{+} MHCII^{+} CD207^{+} LCs among live CD45^{+} cells obtained from fresh epidermal cell suspensions. Data are presented as mean ±SEM, with each point

corresponding to one individual mouse. Statistical analysis was performed using Mann-Whitney U test (ns, $p > 0.05$). **(B)** Representative immunofluorescence staining of $CD207^+$ LCs in ear epidermal sheets of 2-month old mice. Scale bar = 50µm.

Figure S5: ATG5 deficiency does not affect cDC1 homeostasis. (A) Representative dot plots for the identification of $CD207^+$ $CD11b^+$ LCs, $CD207^+$ $CD11b^-$ cDC1, $CD207^-$ $CD11b^+$ cDC2/macrophages and $CD207^-$ $CD11b^-$ (DN, double-negative) DCs among live $CD45^+$ lineage- $CD11c^+$ $MHCII^+$ skin DCs in whole skin cell suspensions from *Atg5*^{WT} and *Atg5*$^{\Delta Cd207}$ mice (lineage markers: B220, NK1.1, Ly6G and CD3). **(B)** Percentages of LCs and cDC1 among skin DCs. Data are presented as mean ±SEM, with each point corresponding to one individual mouse. Statistical analysis was performed using Kruskal-Wallis one-way ANOVA followed by Dunn's multiple comparison test (*, $p<0.05$; ns, $p>0.05$).

Figure S6: ATG5 deficient LCs present ER swelling but no unfolded protein response. (A) Mean fluorescence intensity for ER-tracker on epidermal LCs treated or not with Wortmannin. Data are presented as mean ±SEM, with each point corresponding to one individual mouse. Statistical analysis was performed using Mann-Whitney U test (*, $p<0.05$). **(B)** Representative half-set overlay (left panel) and mean fluorescence intensity (right panel) of ER-tracker in epidermal LCs of control (*Atg5*^{WT} and *Atg5*$^{WT/\Delta}$) and *Atg5*$^{\Delta Cd207}$ mice. Data are presented as mean ±SEM, with each point corresponding to one individual mouse. Statistical analysis was performed using Kruskal-Wallis one-way ANOVA followed by Dunn's multiple comparison test (**, $p<0.01$). **(C)** Representative immunofluorescent stainings of the endoplasmic reticulum using the ER-tracker dye on epidermal LCs *of Atg5*^{WT} **(Supplementary Video SV3)** and *Atg5*$^{\Delta Cd207}$ **(Supplementary Video SV4)** mice. Scale bar: 10µm **(D)** Expression of *Ern1*, total and spliced *Xbp1*, and *Ddit3* mRNAs, in epidermal LCs of control (*Atg5*^{WT} and *Atg5*$^{WT/\Delta}$) and *Atg5*$^{\Delta Cd207}$ mice. Fold changes were calculated relative to mRNA expression in cells of Atg5^{WT} control mice. Data are presented as mean ±SEM, with each point corresponding to one individual mouse. Statistical analysis was performed using Kruskal-Wallis one-way ANOVA followed by Dunn's multiple comparison test (ns, $p>0.05$).

Figure S7: Lack of autophagy alters the transcriptome of Langerhans cells. (A) Visualization of the exon 3 region of *Atg5* gene from RNA-seq of sorted LCs of indicated mouse genotype using integrative Genomic Viewer tool. **(B)** Principal component analysis of RNA-seq transcriptome analysis from sorted LCs of *Atg5*^{WT} and A*tg5*$^{\Delta Cd207}$ mice. **(C)**

Heatmap showing the differentially expressed genes (FDR<0.1, Absolute Log2 Fold Change value > 1, p-value<0.05) between LCs of indicated mouse genotypes **(D)** Volcano plot showing the differential expression of genes between LCs of indicated mouse genotypes. Gene names refer to the top 20 up and downregulated genes, based on the following combinations of p-value and fold-change criteria: blue dots: p-value<0.05 with no cutoff on Absolute Log2 Fold Change; red dots: p-value<0.05 and Absolute Log2 Fold Change value > 1. **(E)** Metascape pathway analysis of genes significantly upregulated or downregulated in *Atg5*$^{\Delta Cd207}$ LCs.

Figure S8: ATG5-deficient LCs do not display defects in mitochondrial function. (A) Representative dot plot of Mitotracker Green and Deep-Red staining and comparison of Mitotracker Deep-Red mean fluorescence intensity of epidermal LCs obtained from control (*Atg5*^{WT} and *Atg5*$^{WT/\Delta}$) and *Atg5*$^{\Delta Cd207}$ mice. **(B)** Representative dot plot of Mitosox Red staining and comparison of Mitosox^{high} percentage of epidermal LCs obtained from control (*Atg5*^{WT} and *Atg5*$^{WT/\Delta}$) and *Atg5*$^{\Delta Cd207}$ mice. Data are presented as mean ±SEM, with each point corresponding to one individual mouse. Statistical analysis was performed using Kruskal-Wallis one-way ANOVA followed by Dunn's multiple comparison test (ns, p>0.05).

Figure S9: Correlation of epidermal nerve and Langerhans cell densities is lost in *Atg5*$^{\Delta Cd207}$ mice. Based on epidermal sheet stainings (Figure 7F-H), the number of CD207^{+} LCs per mm² (X axis) was plotted against the relative areas for β3-tubulin^{+} nerves (Y axis). Linear regressions and R^2 values were calculated for *Atg5*^{WT}, *Atg5*$^{WT/-}$ and *Atg5*$^{\Delta Cd207}$ mice.

Supplementary Video SV1: Autophagosome staining of *Atg5*^{WT} LCs. LC3: green; CD207: red.

Supplementary Video SV2: Endoplasmic reticulum staining of *Atg5*$^{\Delta Cd207}$ LCs. LC3: green; CD207: red.

Supplementary Video SV3: Endoplasmic reticulum staining of *Atg5*^{WT} LCs. CD207: green; ER-tracker: red.

Supplementary Video SV4: Endoplasmic reticulum staining of *Atg5*$^{\Delta Cd207}$ LCs. CD207: green; ER-tracker: red.

Supplementary Video SV5: Lipid droplets of *Atg5*^{WT} LCs. CD207: green; Bodipy: red.

Supplementary Video SV6: Lipid droplets of *Atg5*$^{\Delta Cd207}$ LCs. CD207: green; Bodipy: red.

Bibliography

Agmon, E., J. Solon, P. Bassereau, and B.R. Stockwell. 2018. Modeling the effects of lipid peroxidation during ferroptosis on membrane properties. *Sci Rep*. 8:5155. doi:10.1038/s41598-018-23408-0.

Alissafi, T., A. Banos, L. Boon, T. Sparwasser, A. Ghigo, K. Wing, D. Vassilopoulos, D. Boumpas, T. Chavakis, K. Cadwell, and P. Verginis. 2017. Tregs restrain dendritic cell autophagy to ameliorate autoimmunity. *J Clin.Invest*. 127:2789–2804. doi:10.1172/JCI92079.

Anders, S., P.T. Pyl, and W. Huber. 2015. HTSeq--a Python framework to work with high-throughput sequencing data. *Bioinformatics*. 31:166–169. doi:10.1093/bioinformatics/btu638.

Anding, A.L., and E.H. Baehrecke. 2017. Cleaning House: Selective Autophagy of Organelles. *Dev.Cell*. 41:10–22. doi:10.1016/j.devcel.2017.02.016.

Arbogast, F., J. Arnold, P. Hammann, L. Kuhn, J. Chicher, D. Murera, J. Weishaar, S. Muller, J.D. Fauny, and F. Gros. 2018. ATG5 is required for B cell polarization and presentation of particulate antigens. *Autophagy.* 1–15. doi:10.1080/15548627.2018.1516327.

Arnold, J., D. Murera, F. Arbogast, J.D. Fauny, S. Muller, and F. Gros. 2016. Autophagy is dispensable for B-cell development but essential for humoral autoimmune responses. *Cell Death.Differ.* 23:853–864. doi:10.1038/cdd.2015.149.

Bah, A., and I. Vergne. 2017. Macrophage Autophagy and Bacterial Infections. *Front Immunol.* 8:1483. doi:10.3389/fimmu.2017.01483.

Bedogni, B., S.M. Welford, D.S. Cassarino, B.J. Nickoloff, A.J. Giaccia, and M.B. Powell. 2005. The hypoxic microenvironment of the skin contributes to Akt-mediated melanocyte transformation. *Cancer Cell*. 8:443–454. doi:10.1016/j.ccr.2005.11.005.

Bedoui, S., P.G. Whitney, J. Waithman, L. Eidsmo, L. Wakim, I. Caminschi, R.S. Allan, M. Wojtasiak, K. Shortman, F.R. Carbone, A.G. Brooks, and W.R. Heath. 2009. Cross-presentation of viral and self antigens by skin-derived CD103+ dendritic cells. *Nat.Immunol.* 10:488–495.

Bennett, C.L., E. van Rijn, S. Jung, K. Inaba, R.M. Steinman, M.L. Kapsenberg, and B.E. Clausen. 2005. Inducible ablation of mouse Langerhans cells diminishes but fails to abrogate contact hypersensitivity. *J.Cell.Biol.* 169:569–576.

Bobr, A., B.Z. Igyarto, K.M. Haley, M.O. Li, R.A. Flavell, and D.H. Kaplan. 2012. Autocrine/paracrine TGF-beta1 inhibits Langerhans cell migration. *Proc.Natl.Acad.Sci.U.S.A*. 109:10492–10497. doi:10.1073/pnas.1119178109.

Cavinato, M., R. Koziel, N. Romani, R. Weinmüllner, B. Jenewein, M. Hermann, S. Dubrac, G. Ratzinger, J. Grillari, M. Schmuth, and P. Jansen-Dürr. 2017. UVB-Induced Senescence of Human Dermal Fibroblasts Involves Impairment of Proteasome and Enhanced Autophagic Activity. *J Gerontol A Biol Sci Med Sci*. 72:632–639. doi:10.1093/gerona/glw150.

Chorro, L., A. Sarde, M. Li, K.J. Woollard, P. Chambon, B. Malissen, A. Kissenpfennig, J.B. Barbaroux, R. Groves, and F. Geissmann. 2009. Langerhans cell (LC) proliferation mediates neonatal development, homeostasis, and inflammation-associated expansion of the epidermal LC network. *J Exp Med.* 206:3089–3100. doi:10.1084/jem.20091586.

Clarke, A.J., T. Riffelmacher, D. Braas, R.J. Cornall, and A.K. Simon. 2018. B1a B cells require autophagy for metabolic homeostasis and self-renewal. *J Exp.Med.* 215:399–413. doi:10.1084/jem.20170771.

Clarke, A.J., and A.K. Simon. 2018. Autophagy in the renewal, differentiation and homeostasis of immune cells. *Nat.Rev.Immunol.* doi:10.1038/s41577-018-0095-2.

Cloherty, A.P.M., N.H. van Teijlingen, T.-J.T.H.D. Eisden, J.L. van Hamme, A.G. Rader, T.B.H. Geijtenbeek, R.R.C.E. Schreurs, and C.M.S. Ribeiro. 2021. Autophagy-enhancing drugs limit mucosal HIV-1 acquisition and suppress viral replication ex vivo. *Sci Rep*. 11:4767. doi:10.1038/s41598-021-84081-4.

Cubillos-Ruiz, J.R., P.C. Silberman, M.R. Rutkowski, S. Chopra, A. Perales-Puchalt, M. Song, S. Zhang, S.E. Bettigole, D. Gupta, K. Holcomb, L.H. Ellenson, T. Caputo, A.-H. Lee, J.R. Conejo-Garcia, and L.H. Glimcher. 2015. ER Stress Sensor XBP1 Controls Anti-tumor Immunity by Disrupting Dendritic Cell Homeostasis. *Cell*. 161:1527–1538. doi:10.1016/j.cell.2015.05.025.

Dang, A.T., R.M. Teles, P.T. Liu, A. Choi, A. Legaspi, E.N. Sarno, M.T. Ochoa, K. Parvatiyar, G. Cheng, M. Gilliet, B.R. Bloom, and R.L. Modlin. 2019. Autophagy links antimicrobial activity with antigen presentation in Langerhans cells. *JCI Insight*. 4. doi:10.1172/jci.insight.126955.

Dobin, A., C.A. Davis, F. Schlesinger, J. Drenkow, C. Zaleski, S. Jha, P. Batut, M. Chaisson, and T.R. Gingeras. 2013. STAR: ultrafast universal RNA-seq aligner. *Bioinformatics*. 29:15–21. doi:10.1093/bioinformatics/bts635.

Doebel, T., B. Voisin, and K. Nagao. 2017. Langerhans Cells - The Macrophage in Dendritic Cell Clothing. *Trends Immunol*. 38:817–828. doi:10.1016/j.it.2017.06.008.

Doss, A.L.N., and P.G. Smith. 2014. Langerhans cells regulate cutaneous innervation density and mechanical sensitivity in mouse footpad. *Neurosci Lett*. 578:55–60. doi:10.1016/j.neulet.2014.06.036.

Fayngerts, S.A., J. Wu, C.L. Oxley, X. Liu, A. Vourekas, T. Cathopoulis, Z. Wang, J. Cui, S. Liu, H. Sun, M.A. Lemmon, L. Zhang, Y. Shi, and Y.H. Chen. 2014. TIPE3 is the transfer protein of lipid second messengers that promote cancer. *Cancer Cell*. 26:465–478. doi:10.1016/j.ccr.2014.07.025.

Flacher, V., C.H. Tripp, D.G. Mairhofer, R.M. Steinman, P. Stoitzner, J. Idoyaga, and N. Romani. 2014. Murine Langerin+ dermal dendritic cells prime CD8+ T cells while Langerhans cells induce cross-tolerance. *EMBO Mol Med*. 6:1191–1204. doi:10.15252/emmm.201303283.

Galluzzi, L., F. Pietrocola, B. Levine, and G. Kroemer. 2014. Metabolic control of autophagy. *Cell*. 159:1263–1276. doi:10.1016/j.cell.2014.11.006.

Gao, M., X. Huang, B.-L. Song, and H. Yang. 2019. The biogenesis of lipid droplets: Lipids take center stage. *Prog Lipid Res*. 75:100989. doi:10.1016/j.plipres.2019.100989.

Ghigo, C., I. Mondor, A. Jorquera, J. Nowak, S. Wienert, S.P. Zahner, B.E. Clausen, H. Luche, B. Malissen, F. Klauschen, and M. Bajenoff. 2013. Multicolor fate mapping of Langerhans cell homeostasis. *J Exp Med.* 210:1657–1664. doi:10.1084/jem.20130403.

Ghislat, G., and T. Lawrence. 2018. Autophagy in dendritic cells. *Cell Mol.Immunol.* 15:944–952. doi:10.1038/cmi.2018.2.

Grootjans, J., A. Kaser, R.J. Kaufman, and R.S. Blumberg. 2016. The unfolded protein response in immunity and inflammation. *Nat Rev Immunol*. 16:469–484. doi:10.1038/nri.2016.62.

Hara, T., K. Nakamura, M. Matsui, A. Yamamoto, Y. Nakahara, R. Suzuki-Migishima, M. Yokoyama, K. Mishima, I. Saito, H. Okano, and N. Mizushima. 2006. Suppression of basal autophagy in neural cells causes neurodegenerative disease in mice. *Nature*. 441:885–889. doi:10.1038/nature04724.

Heckmann, B.L., and D.R. Green. 2019. LC3-associated phagocytosis at a glance. *J Cell Sci*. 132. doi:10.1242/jcs.222984.

Henri, S., L.F. Poulin, S. Tamoutounour, L. Ardouin, M. Guilliams, B. de Bovis, E. Devilard, C. Viret, H. Azukizawa, A. Kissenpfennig, and B. Malissen. 2010. CD207+ CD103+ dermal dendritic cells cross-present keratinocyte-derived antigens irrespective of the presence of Langerhans cells. *J.Exp.Med.* 207:189–206.

Herzig, S., and R.J. Shaw. 2018. AMPK: guardian of metabolism and mitochondrial homeostasis. *Nat Rev Mol Cell Biol*. 19:121–135. doi:10.1038/nrm.2017.95.

Hoeffel, G., Y. Wang, M. Greter, P. See, P. Teo, B. Malleret, M. Leboeuf, D. Low, G. Oller, F. Almeida, S.H. Choy, M. Grisotto, L. Renia, S.J. Conway, E.R. Stanley, J.K. Chan, L.G. Ng, I.M. Samokhvalov, M. Merad, and F. Ginhoux. 2012. Adult Langerhans cells derive predominantly from embryonic fetal liver monocytes with a minor contribution of yolk sac-derived macrophages. *J Exp Med.* 209:1167–1181. doi:10.1084/jem.20120340.

Igyarto, B.Z., K. Haley, D. Ortner, A. Bobr, M. Gerami-Nejad, B.T. Edelson, S.M. Zurawski, B. Malissen, G. Zurawski, J. Berman, and D.H. Kaplan. 2011. Skin-resident murine dendritic cell subsets promote distinct and opposing antigen-specific T helper cell responses. *Immunity.* 35:260–272. doi:10.1016/j.immuni.2011.06.005.

Kamath, A.T., S. Henri, F. Battye, D.F. Tough, and K. Shortman. 2002. Developmental kinetics and lifespan of dendritic cells in mouse lymphoid organs. *Blood*. 100:1734–1741.

Kaplan, D.H. 2017. Ontogeny and function of murine epidermal Langerhans cells. *Nat.Immunol.* 18:1068–1075. doi:10.1038/ni.3815.

Kaplan, D.H., M.O. Li, M.C. Jenison, W.D. Shlomchik, R.A. Flavell, and M.J. Shlomchik. 2007. Autocrine/paracrine TGFbeta1 is required for the development of epidermal Langerhans cells. *J.Exp.Med.* 204:2545–2552.

Kashem, S.W., B.Z. Igyarto, M. Gerami-Nejad, Y. Kumamoto, J. Mohammed, E. Jarrett, R.A. Drummond, S.M. Zurawski, G. Zurawski, J. Berman, A. Iwasaki, G.D. Brown, and D.H. Kaplan. 2015. Candida albicans Morphology and Dendritic Cell Subsets Determine T Helper Cell Differentiation. *Immunity.* 42:356–366. doi:10.1016/j.immuni.2015.01.008.

Kel, J.M., M.J.H. Girard-Madoux, B. Reizis, and B.E. Clausen. 2010. TGF-beta is required to maintain the pool of immature Langerhans cells in the epidermis. *J Immunol*. 185:3248–3255. doi:10.4049/jimmunol.1000981.

Kellersch, B., and T. Brocker. 2013. Langerhans cell homeostasis in mice is dependent on mTORC1 but not mTORC2 function. *Blood*. 121:298–307. doi:10.1182/blood-2012-06-439786.

Kim, S.J., G.H. Syed, M. Khan, W.W. Chiu, M.A. Sohail, R.G. Gish, and A. Siddiqui. 2014. Hepatitis C virus triggers mitochondrial fission and attenuates apoptosis to promote viral persistence. *Proc.Natl.Acad.Sci.U.S.A*. 111:6413–6418. doi:10.1073/pnas.1321114111.

Kolter, J., R. Feuerstein, P. Zeis, N. Hagemeyer, N. Paterson, P. d'Errico, S. Baasch, L. Amann, T. Masuda, A. Losslein, K. Gharun, M. Meyer-Luehmann, C. Waskow, C.W. Franzke, D. Grun, T. Lammermann, M. Prinz, and P. Henneke. 2019. A Subset of Skin Macrophages Contributes to the Surveillance and Regeneration of Local Nerves. *Immunity.* 50:1482–1497. doi:10.1016/j.immuni.2019.05.009.

Kounakis, K., M. Chaniotakis, M. Markaki, and N. Tavernarakis. 2019. Emerging Roles of Lipophagy in Health and Disease. *Front Cell Dev Biol*. 7:185. doi:10.3389/fcell.2019.00185.

Langmead, B., and S.L. Salzberg. 2012. Fast gapped-read alignment with Bowtie 2. *Nat Methods*. 9:357–359. doi:10.1038/nmeth.1923.

Lee, H.K., L.M. Mattei, B.E. Steinberg, P. Alberts, Y.H. Lee, A. Chervonsky, N. Mizushima, S. Grinstein, and A. Iwasaki. 2010. In vivo requirement for Atg5 in antigen presentation by dendritic cells. *Immunity.* 32:227–239.

Liang, J., S.H. Shao, Z.-X. Xu, B. Hennessy, Z. Ding, M. Larrea, S. Kondo, D.J. Dumont, J.U. Gutterman, C.L. Walker, J.M. Slingerland, and G.B. Mills. 2007. The energy sensing LKB1–AMPK pathway regulates p27kip1 phosphorylation mediating the decision to enter autophagy or apoptosis. *Nat Cell Biol*. 9:218–224. doi:10.1038/ncb1537.

Love, M.I., W. Huber, and S. Anders. 2014. Moderated estimation of fold change and dispersion for RNA-seq data with DESeq2. *Genome Biol*. 15:550. doi:10.1186/s13059-014-0550-8.

Merad, M., M.G. Manz, H. Karsunky, A. Wagers, W. Peters, I. Charo, I.L. Weissman, J.G. Cyster, and E.G. Engleman. 2002. Langerhans cells renew in the skin throughout life under steady-state conditions. *Nat.Immunol.* 3:1135–1141.

Mintern, J.D., C. Macri, W.J. Chin, S.E. Panozza, E. Segura, N.L. Patterson, P. Zeller, D. Bourges, S. Bedoui, P.J. McMillan, A. Idris, C.J. Nowell, A. Brown, K.J. Radford, A.P. Johnston, and J.A. Villadangos. 2015. Differential use of autophagy by primary dendritic cells specialized in cross-presentation. *Autophagy.* 11:906–917. doi:10.1080/15548627.2015.1045178.

Müller, G., C. Lübow, and G. Weindl. 2020. Lysosomotropic beta blockers induce oxidative stress and IL23A production in Langerhans cells. *Autophagy*. 16:1380–1395. doi:10.1080/15548627.2019.1686728.

Munz, C. 2015. Of LAP, CUPS, and DRibbles - Unconventional Use of Autophagy Proteins for MHC Restricted Antigen Presentation. *Front Immunol*. 6:200. doi:10.3389/fimmu.2015.00200.

Murera, D., F. Arbogast, J. Arnold, D. Bouis, S. Muller, and F. Gros. 2018. CD4 T cell autophagy is integral to memory maintenance. *Sci.Rep.* 8:5951. doi:10.1038/s41598-018-23993-0.

Oh, D.S., and H.K. Lee. 2019. Autophagy protein ATG5 regulates CD36 expression and anti-tumor MHC class II antigen presentation in dendritic cells. *Autophagy*. 15:2091–2106. doi:10.1080/15548627.2019.1596493.

Parekh, V.V., S.K. Pabbisetty, L. Wu, E. Sebzda, J. Martinez, J. Zhang, and K.L. Van. 2017. Autophagy-related protein Vps34 controls the homeostasis and function of antigen cross-presenting CD8alpha(+) dendritic cells. *Proc.Natl.Acad.Sci.U.S.A*. 114:E6371–E6380. doi:10.1073/pnas.1706504114.

Pengo, N., M. Scolari, L. Oliva, E. Milan, F. Mainoldi, A. Raimondi, C. Fagioli, A. Merlini, E. Mariani, E. Pasqualetto, U. Orfanelli, M. Ponzoni, R. Sitia, S. Casola, and S. Cenci. 2013. Plasma cells require autophagy for sustainable immunoglobulin production. *Nat Immunol*. 14:298–305. doi:10.1038/ni.2524.

Pierobon, D., F. Raggi, I. Cambieri, S. Pelassa, S. Occhipinti, P. Cappello, F. Novelli, T. Musso, A. Eva, C. Castagnoli, L. Varesio, M. Giovarelli, and M.C. Bosco. 2016. Regulation of Langerhans cell functions in a hypoxic environment. *J Mol.Med.(Berl)*. 94:943–955. doi:10.1007/s00109-016-1400-9.

Price, J.G., J. Idoyaga, H. Salmon, B. Hogstad, C.L. Bigarella, S. Ghaffari, M. Leboeuf, and M. Merad. 2015. CDKN1A regulates Langerhans cell survival and promotes Treg cell generation upon exposure to ionizing irradiation. *Nat.Immunol.* 16:1060–1068. doi:10.1038/ni.3270.

Ribeiro, C.M., R. Sarrami-Forooshani, L.C. Setiawan, E.M. Zijlstra-Willems, J.L. van Hamme, W. Tigchelaar, N.N. Van der Wel, N.A. Kootstra, S.I. Gringhuis, and T.B. Geijtenbeek. 2016. Receptor usage dictates HIV-1 restriction by human TRIM5alpha in dendritic cell subsets. *Nature*. 540:448–452. doi:10.1038/nature20567.

Riffelmacher, T., A. Clarke, F.C. Richter, A. Stranks, S. Pandey, S. Danielli, P. Hublitz, Z. Yu, E. Johnson, T. Schwerd, J. McCullagh, H. Uhlig, S.E.W. Jacobsen, and A.K. Simon. 2017. Autophagy-Dependent Generation of Free Fatty Acids Is Critical for Normal Neutrophil Differentiation. *Immunity*. 47:466-480.e5. doi:10.1016/j.immuni.2017.08.005.

Said, A., S. Bock, T. Lajqi, G. Müller, and G. Weindl. 2014. Chloroquine promotes IL-17 production by CD4+ T cells via p38-dependent IL-23 release by monocyte-derived Langerhans-like cells. *J Immunol*. 193:6135–6143. doi:10.4049/jimmunol.1303276.

Schuler, G., and R.M. Steinman. 1985. Murine epidermal Langerhans cells mature into potent immunostimulatory dendritic cells in vitro. *J.Exp.Med.* 161:526–546.

Sil, P., J. Suwanpradid, G. Muse, A. Gruzdev, L. Liu, D.L. Corcoran, C.J. Willson, K. Janardhan, S. Grimm, P. Myers, L.M. Degraff, A.S. MacLeod, and J. Martinez. 2020. Noncanonical autophagy in dermal dendritic cells mediates immunosuppressive effects of UV exposure. *J Allergy Clin Immunol*. 145:1389–1405. doi:10.1016/j.jaci.2019.11.041.

Singh, T.P., H.H. Zhang, I. Borek, P. Wolf, M.N. Hedrick, S.P. Singh, B.L. Kelsall, B.E. Clausen, and J.M. Farber. 2016. Monocyte-derived inflammatory Langerhans cells and dermal dendritic cells mediate psoriasis-like inflammation. *Nat Commun*. 7:13581. doi:10.1038/ncomms13581.

Song, S., J. Tan, Y. Miao, and Q. Zhang. 2018. Crosstalk of ER stress-mediated autophagy and ER-phagy: Involvement of UPR and the core autophagy machinery. *J Cell Physiol*. 233:3867–3874. doi:10.1002/jcp.26137.

Sparber, F., J.M. Scheffler, N. Amberg, C.H. Tripp, V. Heib, M. Hermann, S.P. Zahner, B.E. Clausen, B. Reizis, L.A. Huber, P. Stoitzner, and N. Romani. 2014. The late endosomal adaptor molecule p14 (LAMTOR2) represents a novel regulator of Langerhans cell homeostasis. *Blood*. 123:217–227. doi:10.1182/blood-2013-08-518555.

Sparber, F., C.H. Tripp, K. Komenda, J.M. Scheffler, B.E. Clausen, L.A. Huber, N. Romani, and P. Stoitzner. 2015. The late endosomal adaptor molecule p14 (LAMTOR2) regulates TGFbeta1-mediated homeostasis of Langerhans cells. *J Invest Dermatol.* 135:119–129. doi:10.1038/jid.2014.324.

Stockwell, B.R. 2022. Ferroptosis turns 10: Emerging mechanisms, physiological functions, and therapeutic applications. *Cell*. 185:2401–2421. doi:10.1016/j.cell.2022.06.003.

Su, Q., A. Bouteau, J. Cardenas, B. Uthra, Y. Wang, C. Smitherman, J. Gu, and B.Z. Igyártó. 2020. Brief communication: Long-term absence of Langerhans cells alters the gene expression profile of keratinocytes and dendritic epidermal T cells. *PLoS One*. 15:e0223397. doi:10.1371/journal.pone.0223397.

Takahama, M., S. Akira, and T. Saitoh. 2018. Autophagy limits activation of the inflammasomes. *Immunol Rev*. 281:62–73. doi:10.1111/imr.12613.

Tavernier, S.J., F. Osorio, L. Vandersarren, J. Vetters, N. Vanlangenakker, I.G. Van, K. Vergote, R.R. De, E. Parthoens, L. van de Laar, T. Iwawaki, J.R. Del Valle, C.C. Hu,

B.N. Lambrecht, and S. Janssens. 2017. Regulated IRE1-dependent mRNA decay sets the threshold for dendritic cell survival. *Nat.Cell Biol.* 19:698–710. doi:10.1038/ncb3518.

Tripp, C.H., S. Chang-Rodriguez, P. Stoitzner, S. Holzmann, H. Stössel, P. Douillard, S. Saeland, F. Koch, A. Elbe-Bürger, and N. Romani. 2004. Ontogeny of Langerin/CD207 expression in the epidermis of mice. *J.Invest.Dermatol.* 122:670–672.

Valecka, J., C.R. Almeida, B. Su, P. Pierre, and E. Gatti. 2018. Autophagy and MHC-restricted antigen presentation. *Mol Immunol*. 99:163–170. doi:10.1016/j.molimm.2018.05.009.

Velázquez, A.P., T. Tatsuta, R. Ghillebert, I. Drescher, and M. Graef. 2016. Lipid droplet-mediated ER homeostasis regulates autophagy and cell survival during starvation. *J Cell Biol*. 212:621–631. doi:10.1083/jcb.201508102.

Voisin, B., D. Chartoire, C. Devouassoux, C. Kowalczyk-Quintas, F. Clauss, F. Lezot, P. Schneider, V. Flacher, and C.G. Mueller. 2019. The hair cycle underlies regulation of Langerhans cell renewal. *bioRxiv*. 832774. doi:10.1101/832774.

Weindel, C.G., L.J. Richey, A.J. Mehta, M. Shah, and B.T. Huber. 2017. Autophagy in Dendritic Cells and B Cells Is Critical for the Inflammatory State of TLR7-Mediated Autoimmunity. *J Immunol*. 198:1081–1092. doi:10.4049/jimmunol.1601307.

Wu, M.-Y., and J.-H. Lu. 2019. Autophagy and Macrophage Functions: Inflammatory Response and Phagocytosis. *Cells*. 9:E70. doi:10.3390/cells9010070.

Xia, H., S. Li, X. Li, W. Wang, Y. Bian, S. Wei, S. Grove, W. Wang, L. Vatan, J.R. Liu, K. McLean, R. Rattan, A. Munkarah, J.-L. Guan, I. Kryczek, and W. Zou. 2020. Autophagic adaptation to oxidative stress alters peritoneal residential macrophage survival and ovarian cancer metastasis. *JCI Insight*. 5:141115. doi:10.1172/jci.insight.141115.

Xu, X., K. Araki, S. Li, J.H. Han, L. Ye, W.G. Tan, B.T. Konieczny, M.W. Bruinsma, J. Martinez, E.L. Pearce, D.R. Green, D.P. Jones, H.W. Virgin, and R. Ahmed. 2014. Autophagy is essential for effector CD8(+) T cell survival and memory formation. *Nat Immunol*. 15:1152–61. doi:10.1038/ni.3025.

Zahner, S.P., J.M. Kel, C.A. Martina, I. Brouwers-Haspels, M.A. van Roon, and B.E. Clausen. 2011. Conditional deletion of TGF-betaR1 using Langerin-Cre mice results in Langerhans cell deficiency and reduced contact hypersensitivity. *J.Immunol.* 187:5069–5076.

Zhang, S., T.N. Edwards, V.K. Chaudhri, J. Wu, J.A. Cohen, T. Hirai, N. Rittenhouse, E.G. Schmitz, P.Y. Zhou, B.D. McNeil, Y. Yang, H.R. Koerber, T.L. Sumpter, A.C. Poholek, B.M. Davis, K.M. Albers, H. Singh, and D.H. Kaplan. 2021. Nonpeptidergic neurons suppress mast cells via glutamate to maintain skin homeostasis. *Cell*. 184:2151-2166.e16. doi:10.1016/j.cell.2021.03.002.

Zhang, X., X. Li, Y. Wang, Y. Chen, Y. Hu, C. Guo, Z. Yu, P. Xu, Y. Ding, Q.-S. Mi, J. Wu, J. Gu, and Y. Shi. 2022. Abnormal lipid metabolism in epidermal Langerhans cells

mediates psoriasis-like dermatitis. *JCI Insight*. 7:e150223. doi:10.1172/jci.insight.150223.

Zhou, Y., B. Zhou, L. Pache, M. Chang, A.H. Khodabakhshi, O. Tanaseichuk, C. Benner, and S.K. Chanda. 2019. Metascape provides a biologist-oriented resource for the analysis of systems-level datasets. *Nat Commun*. 10:1523. doi:10.1038/s41467-019-09234-6.

Figure 1: ATG5 deficiency in Langerhans cells disrupts autophagosomes and depletes their epidermal network.

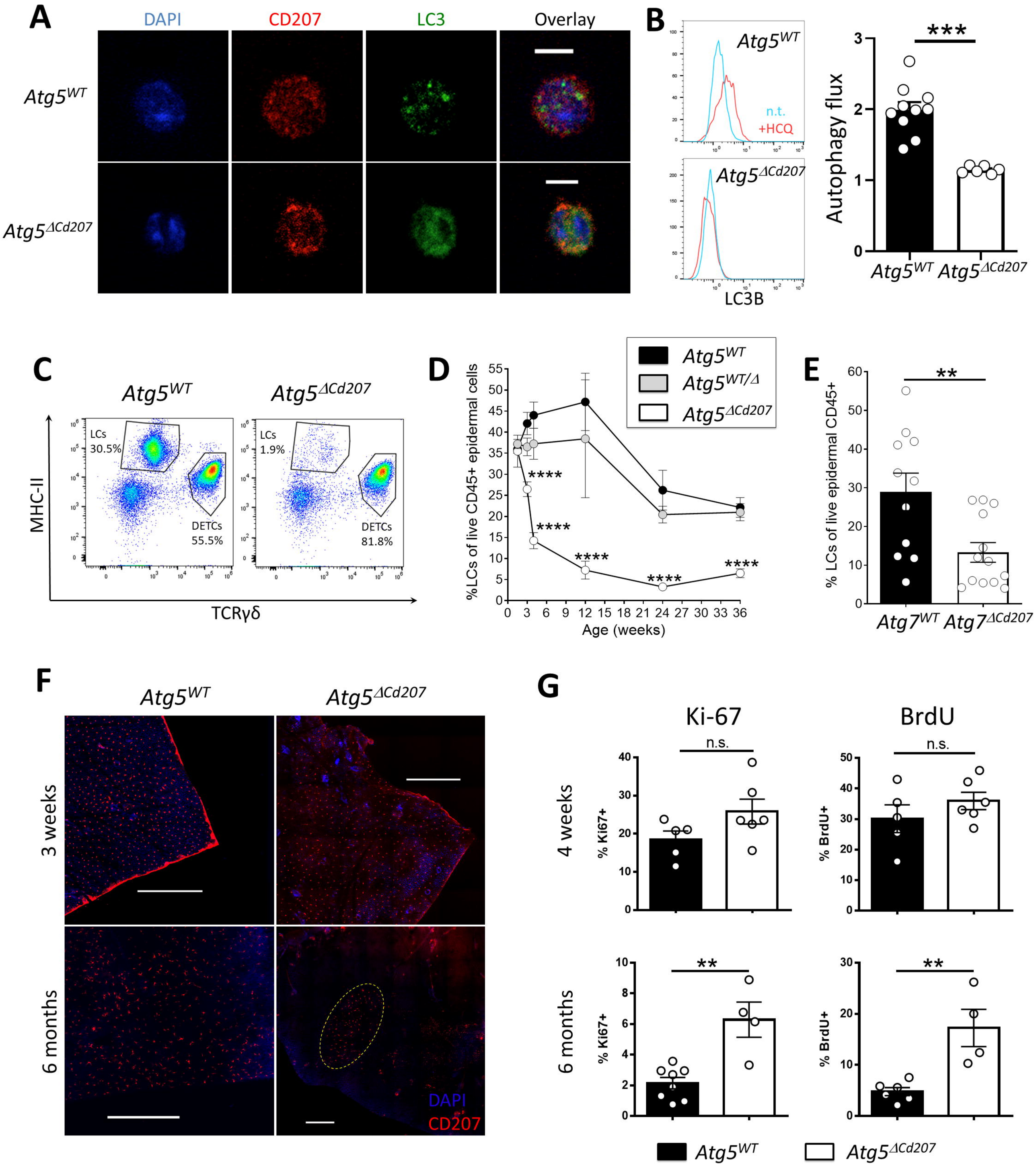

Figure 2: ATG5-deficient LCs are more prone to apoptosis.

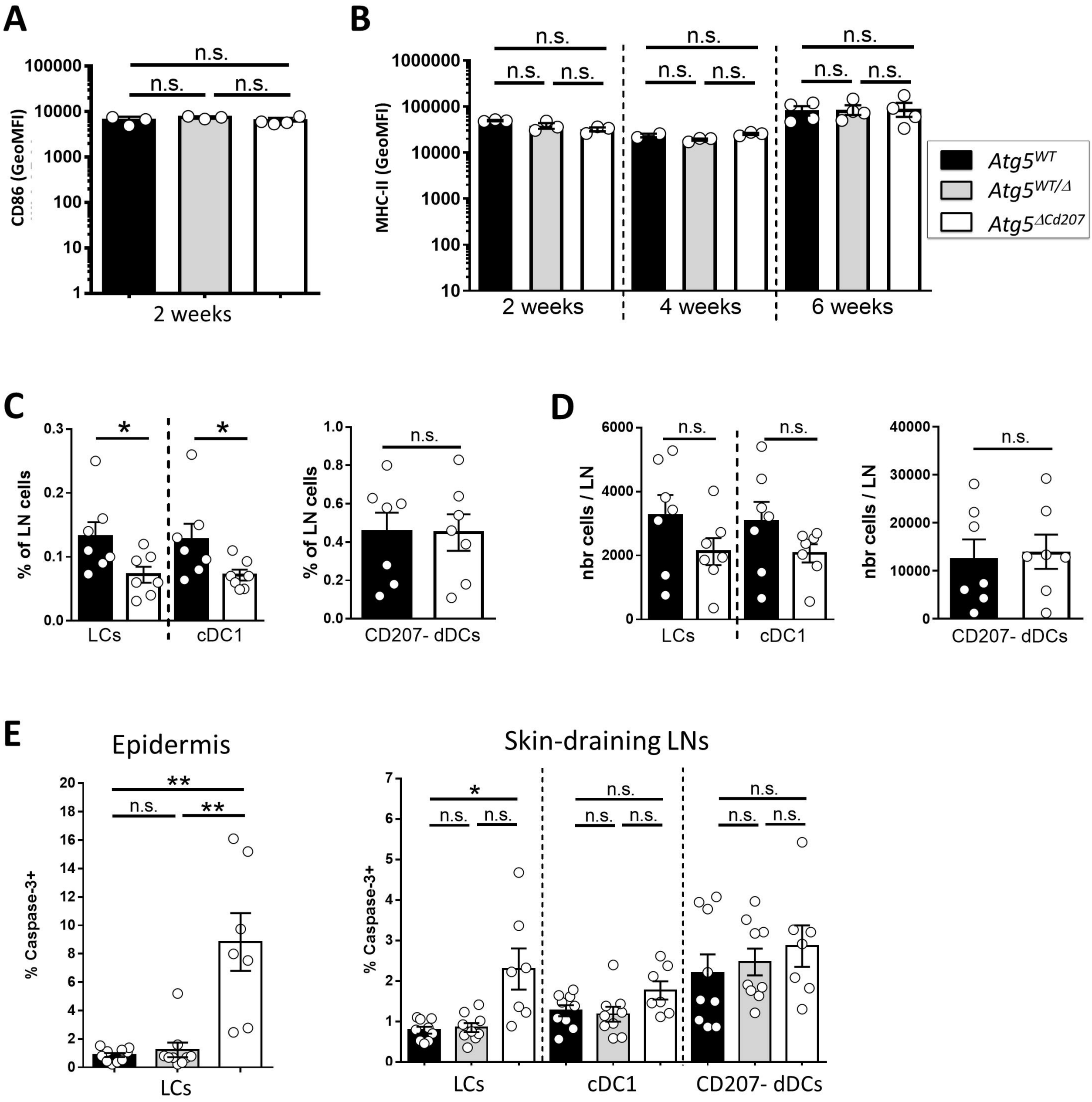

Figure 3: Impaired autophagy increases the lipid storage compartments of Langerhans cells.

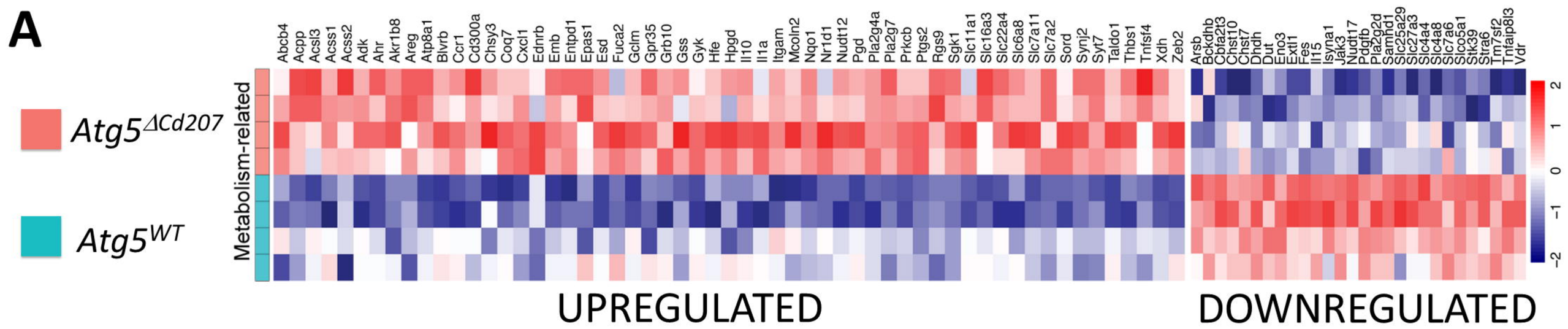

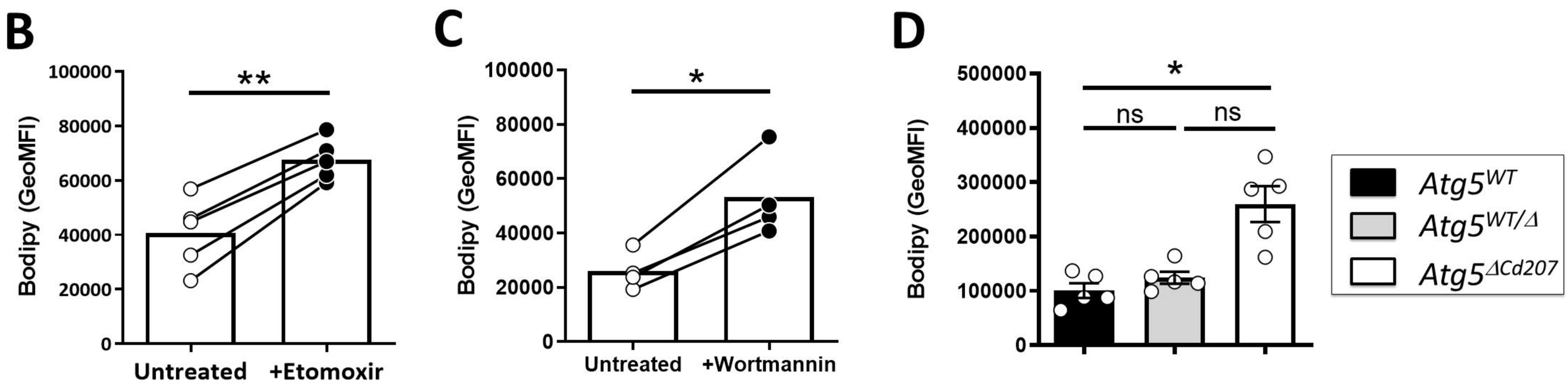

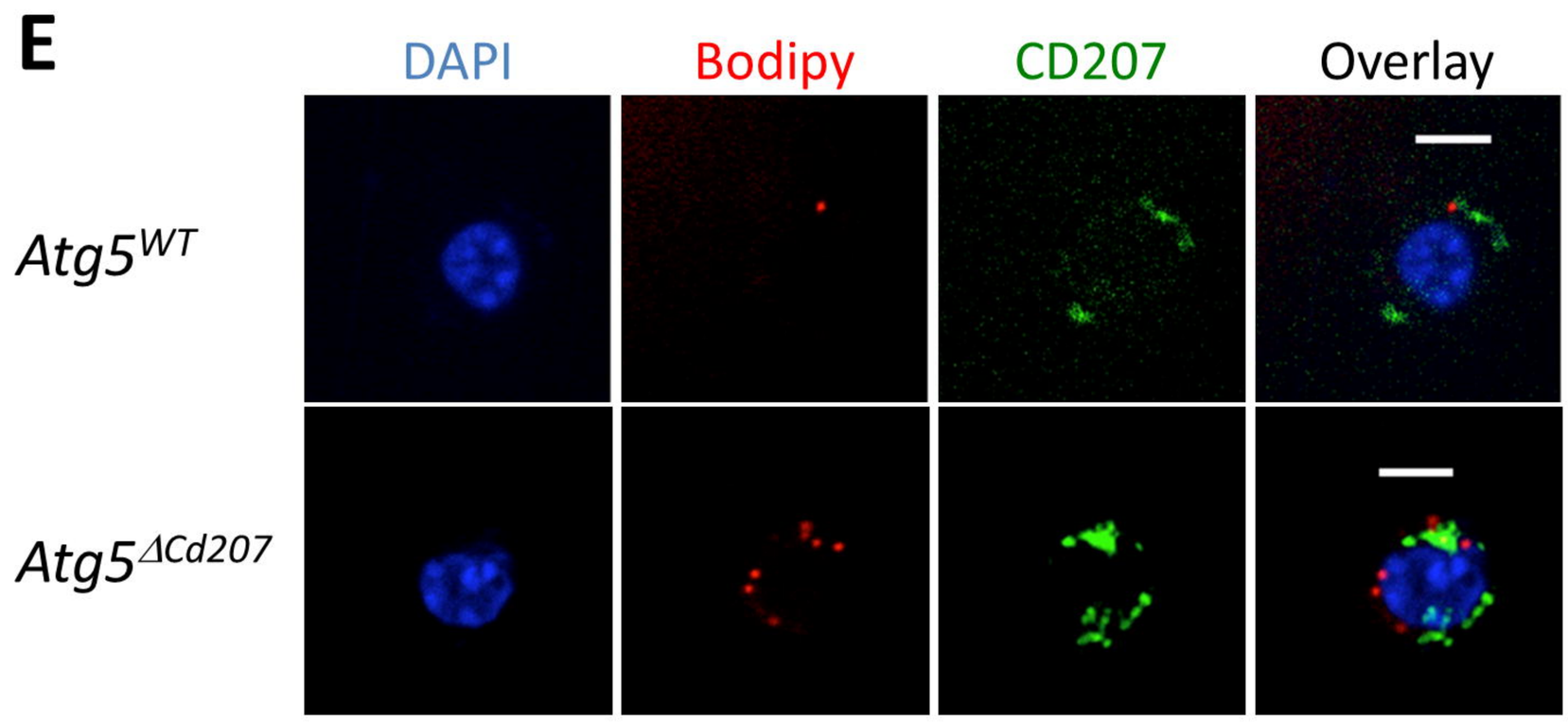

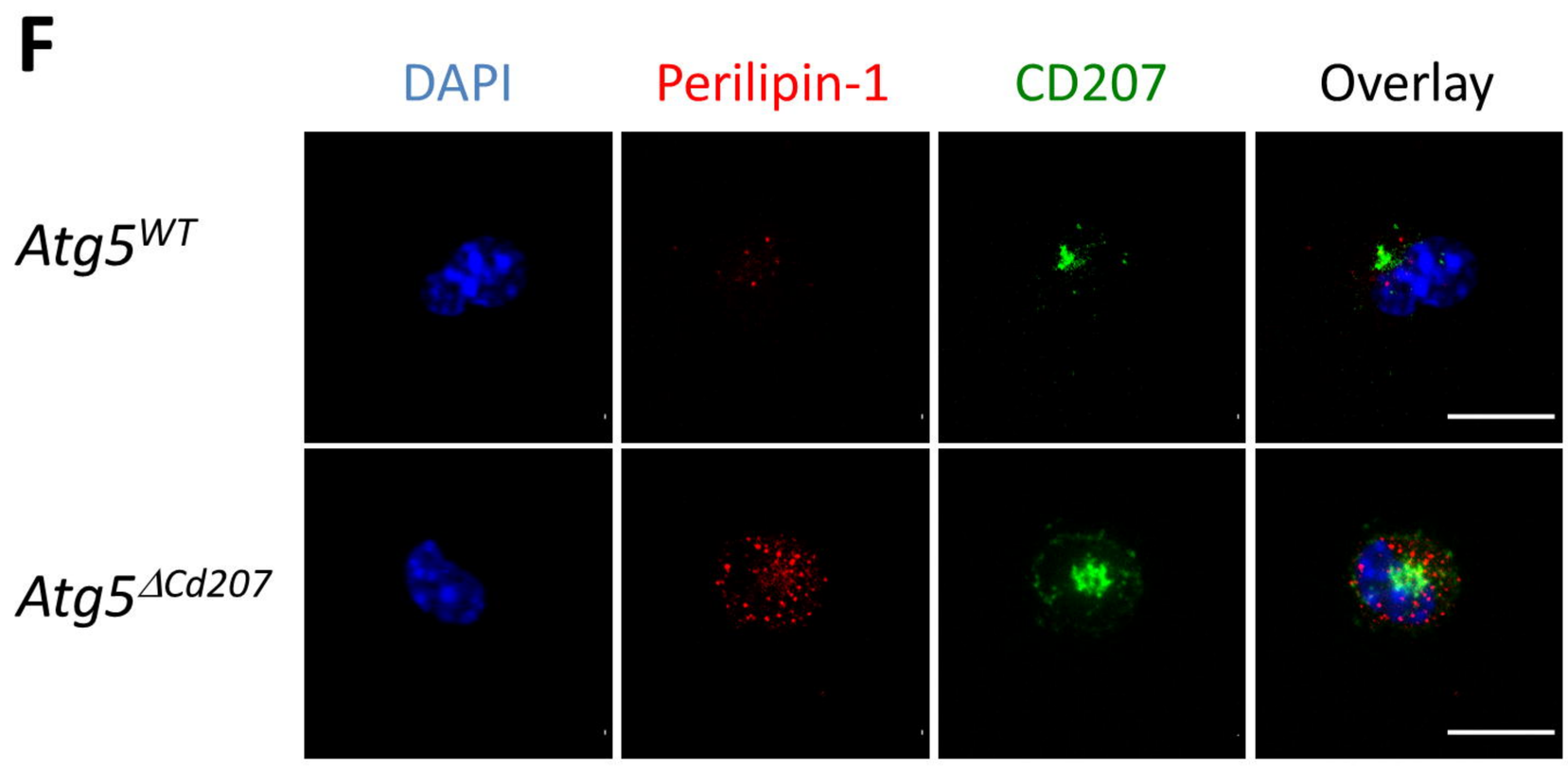

Figure 4: Impaired lipid metabolism leads ATG5-deficient LCs to ferroptosis

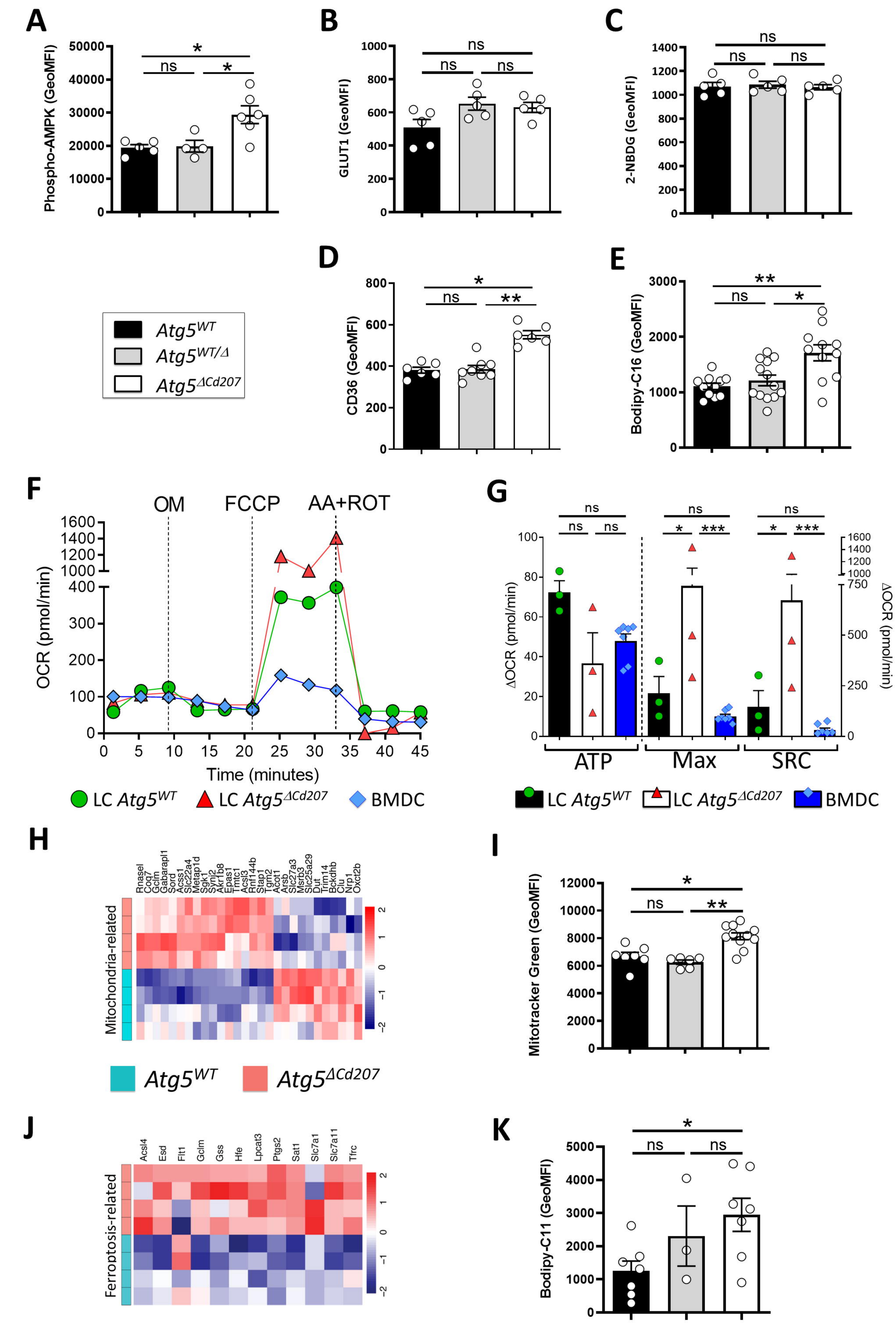
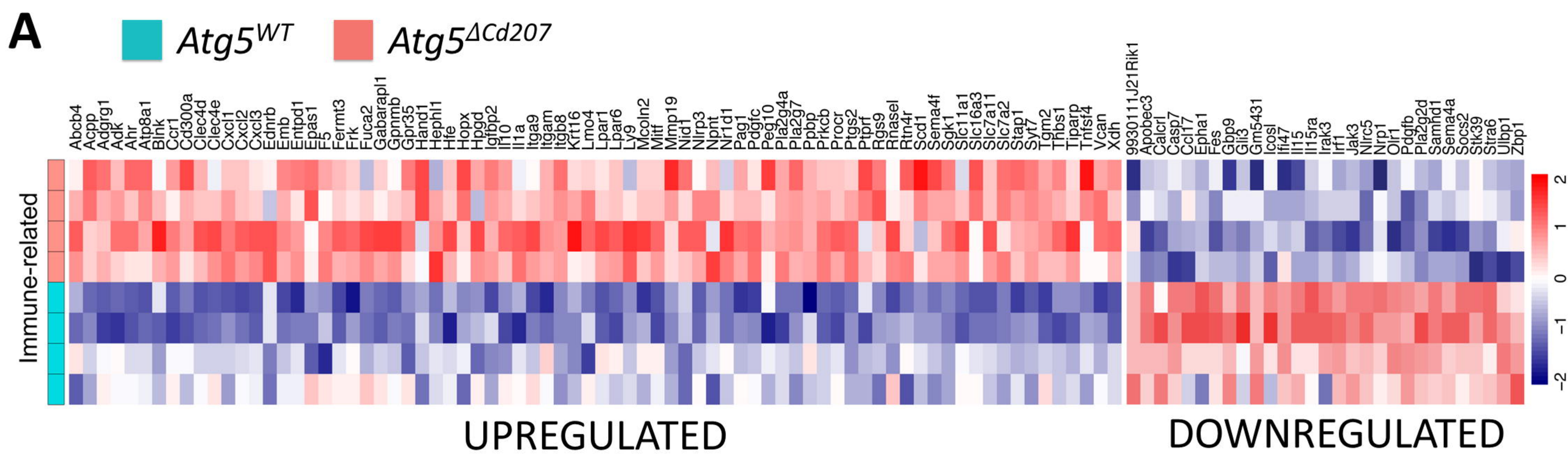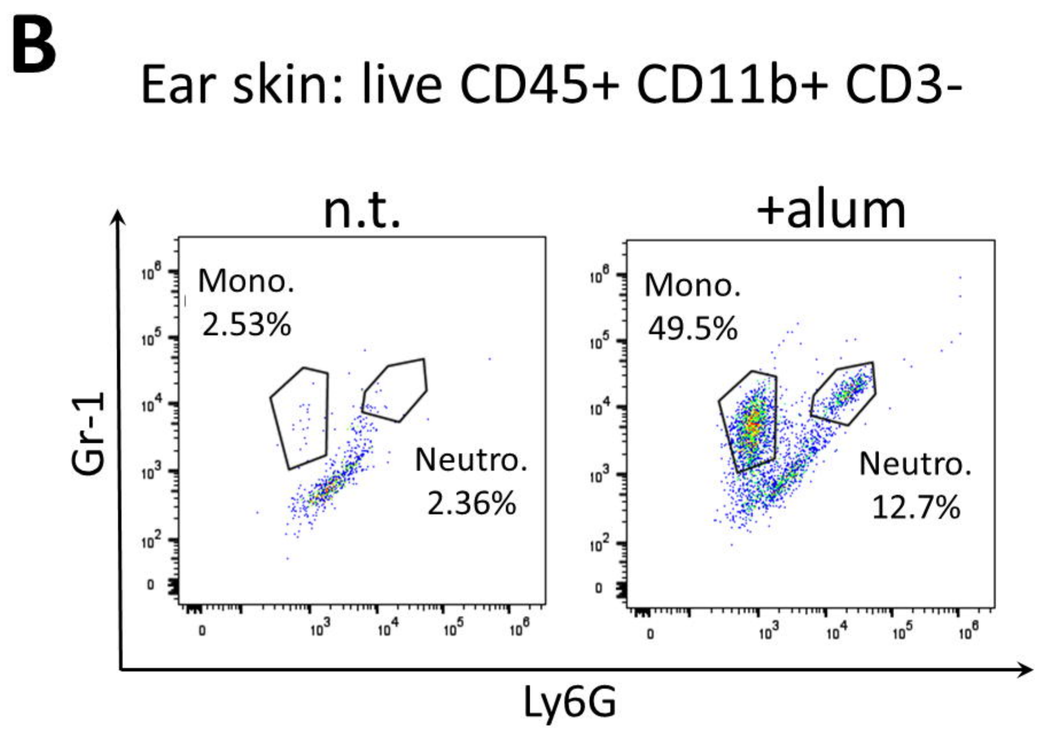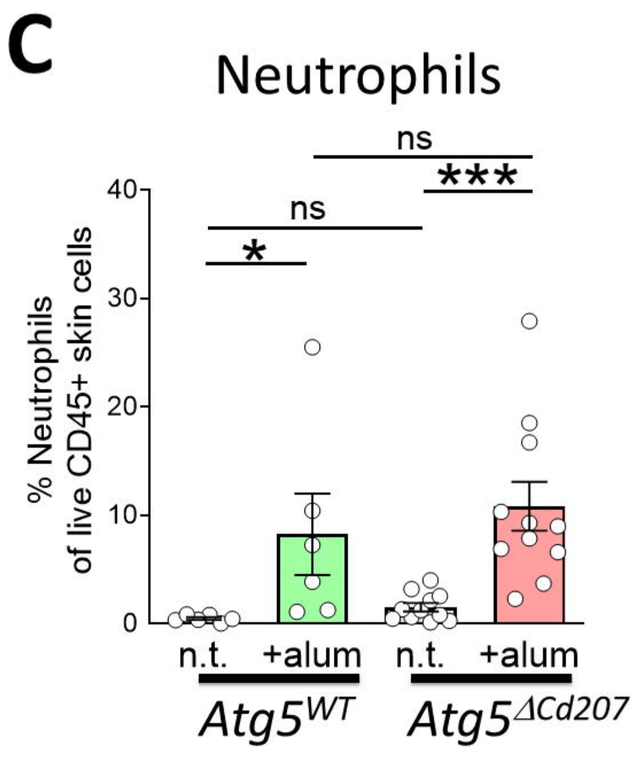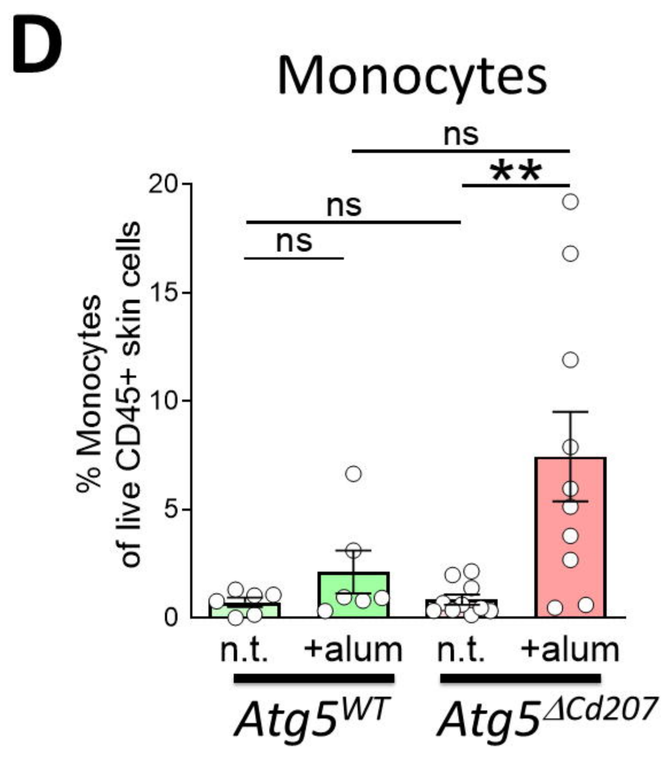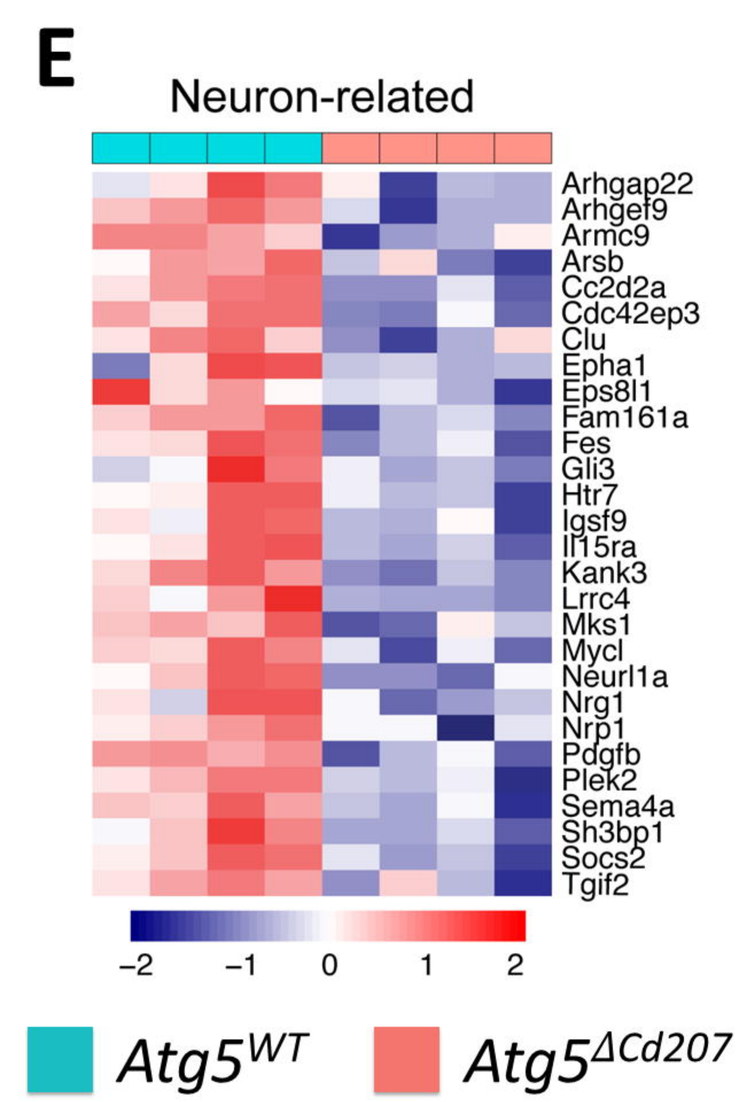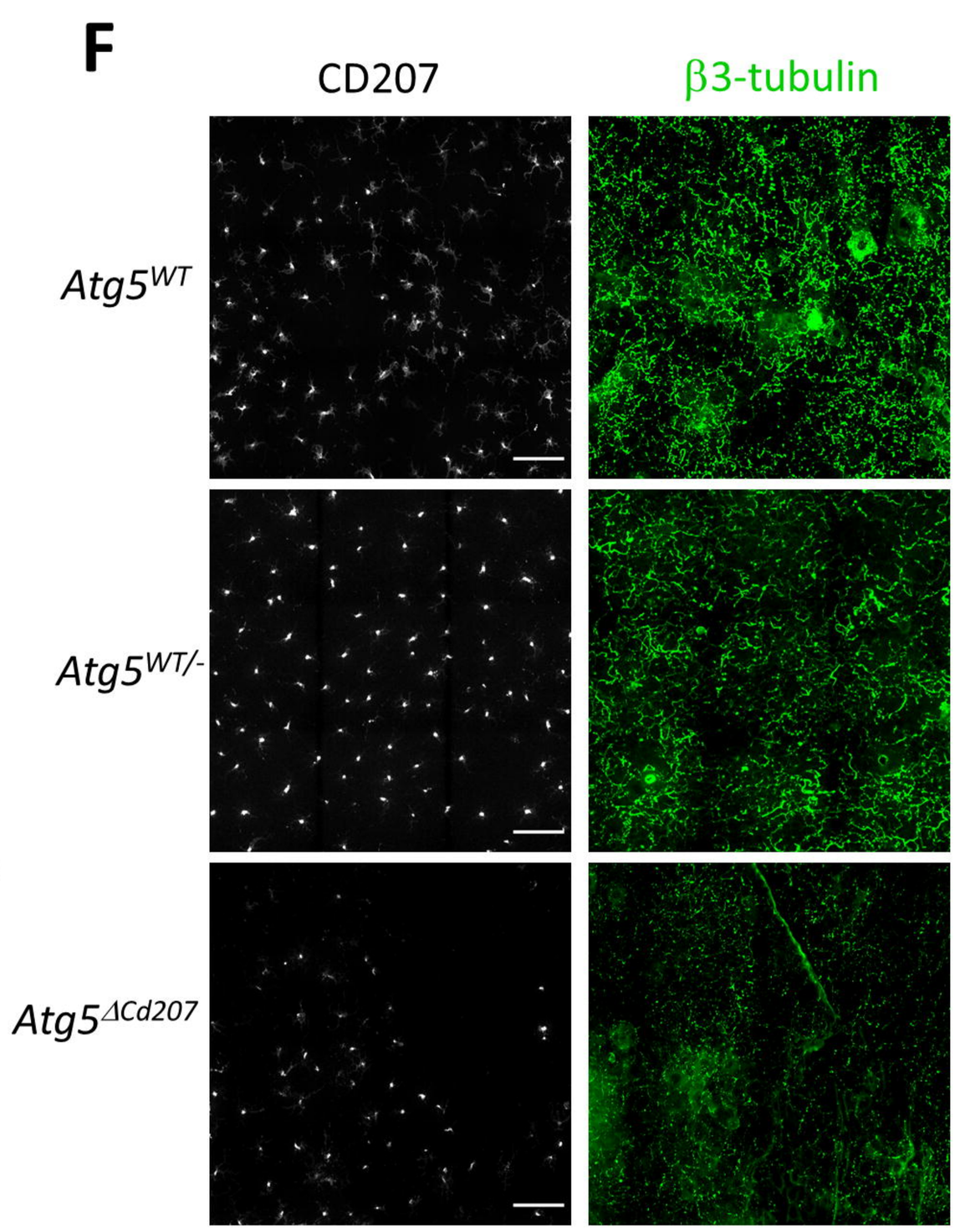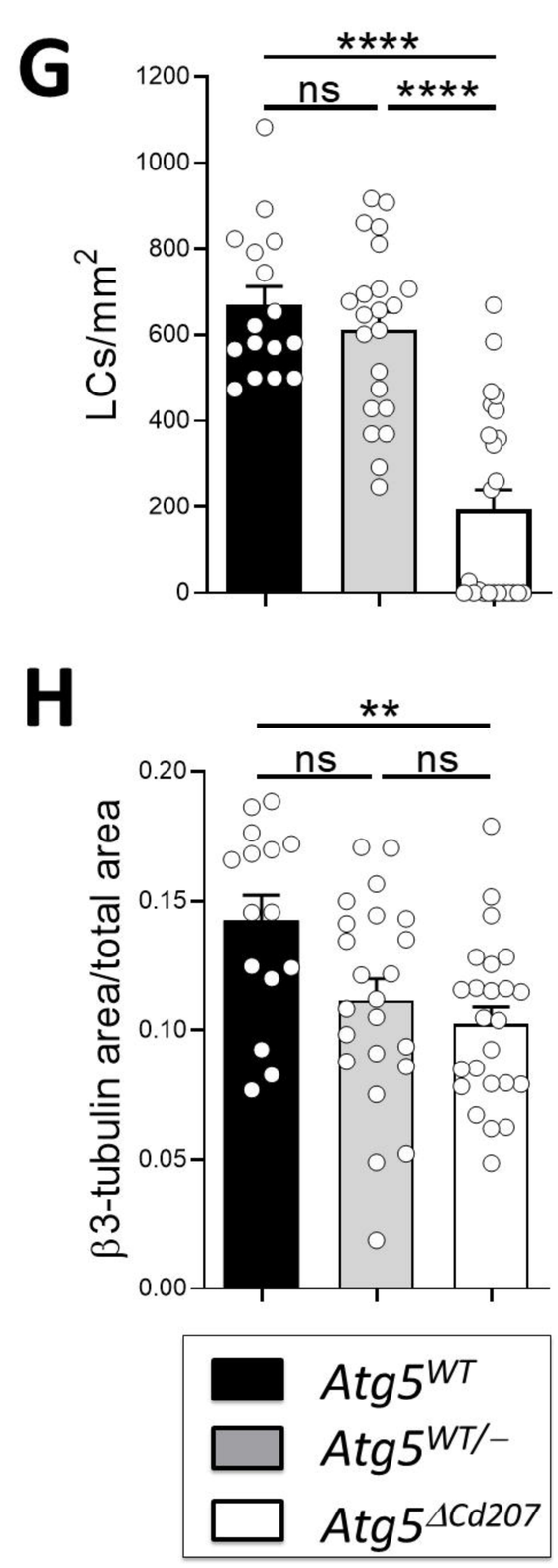
Fig 5 LCs under metabolic stress have impaired tissue homeostasis functior